A Little Data goes a Long Way: Automating Seismic Phase Arrival Picking at Nabro Volcano with Transfer Learning

Sacha Lapins[1,1], Berhe Goitom[1,1], J.-Michael Kendall[2,2], Maximilian J. Werner[1,1], Katharine V. Cashman[1,1], and James Hammond[3,3]

[1]University of Bristol
[2]University of Oxford
[3]Birkbeck, University of London

November 30, 2022

Abstract

Supervised deep learning models have become a popular choice for seismic phase arrival detection. However, they don't always perform well on out-of-distribution data and require large training sets to aid generalization and prevent overfitting. This can present issues when using these models in new monitoring settings. In this work, we develop a deep learning model for automating phase arrival detection at Nabro volcano using a limited amount of training data (2498 event waveforms recorded over 35 days) through a process known as transfer learning. We use the feature extraction layers of an existing, extensively-trained seismic phase picking model to form the base of a new all-convolutional model, which we call U-GPD. We demonstrate that transfer learning reduces overfitting and model error relative to training the same model from scratch, particularly for small training sets (e.g., 500 waveforms). The new U-GPD model achieves greater classification accuracy and smaller arrival time residuals than off-the-shelf applications of two existing, extensively-trained baseline models for a test set of 800 event and noise waveforms from Nabro volcano. When applied to 14 months of continuous Nabro data, the new U-GPD model detects 31,387 events with at least four P-wave arrivals and one S-wave arrival, which is more than the original base model (26,808 events) and our existing manual catalogue (2,926 events), with smaller location errors. The new model is also more efficient when applied as a sliding window, processing 14 months of data from 7 stations in less than 4 hours on a single GPU.

A Little Data goes a Long Way: Automating Seismic Phase Arrival Picking at Nabro Volcano with Transfer Learning

Enter authors here: Sacha Lapins[1], Berhe Goitom[1], J-Michael Kendall[2], Maximilian J. Werner[1], Katharine V. Cashman[1] and James O. S. Hammond[3]

[1]School of Earth Sciences, University of Bristol, UK.

[2]Department of Earth Sciences, University of Oxford, UK.

[3]Department of Earth and Planetary Sciences, Birkbeck, University of London, UK.

Corresponding author: Sacha Lapins (sacha.lapins@bristol.ac.uk)

Key Points:

- Transfer learning using existing model trained on California earthquake data produces effective new model for monitoring at Nabro volcano
- Nabro transfer learning model shows improved S-wave picking resulting in smaller location errors than even manual phase picks
- Changing task from classification to segmentation results in more efficient model processing 14 months of data from 7 stations in 4 hours

Abstract

Supervised deep learning models have become a popular choice for seismic phase arrival detection. However, they don't always perform well on out-of-distribution data and require large training sets to aid generalization and prevent overfitting. This can present issues when using these models in new monitoring settings. In this work, we develop a deep learning model for automating phase arrival detection at Nabro volcano using a limited amount of training data (2498 event waveforms recorded over 35 days) through a process known as transfer learning. We use the feature extraction layers of an existing, extensively-trained seismic phase picking model to form the base of a new all-convolutional model, which we call U-GPD. We demonstrate that transfer learning reduces overfitting and model error relative to training the same model from scratch, particularly for small training sets (e.g., 500 waveforms). The new U-GPD model achieves greater classification accuracy and smaller arrival time residuals than off-the-shelf applications of two existing, extensively-trained baseline models for a test set of 800 event and noise waveforms from Nabro volcano. When applied to 14 months of continuous Nabro data, the new U-GPD model detects 31,387 events with at least four P-wave arrivals and one S-wave arrival, which is more than the original base model (26,808 events) and our existing manual catalogue (2,926 events), with smaller location errors. The new model is also more efficient when applied as a sliding window, processing 14 months of data from 7 stations in less than 4 hours on a single GPU.

Plain Language Summary

Seismic monitoring increasingly relies on automated signal processing as the rate of data acquisition grows. Supervised deep learning models have proven to be effective for detecting and characterizing seismic events, but training such highly parameterized models generally requires large amounts of manually labelled data. Once trained, however, these models extract general seismic waveform features that can be used to train new models with more limited training data. In this work, we use the generalized knowledge of seismic data from a model trained on millions of earthquakes in California to train a new model for detecting volcanic earthquakes at Nabro volcano, Eritrea, a recently active and, prior to its 2011 eruption, poorly monitored volcano. Using

a small training set of waveforms, the new model more accurately detects phase arrivals and noise than off-the-shelf applications of two baseline models. The new model is efficient, processing 14 months of data in less than 4 hours. It is also effective, detecting more volcanic events and showing improved levels of S-wave arrival picking. The result is smaller event location errors than even our manual picks. This level of efficiency and consistency highlights the role that machine learning can play in volcano-seismic monitoring.

1 Introduction

Seismic monitoring plays a fundamental part in mitigating hazards at volcanoes. During periods of unrest, thousands of earthquakes can occur each day, producing a diverse range of seismic signals that reflect a multitude of interlinked volcanic processes (e.g., migrating fluids, fault movement, explosions, rockfalls). These earthquakes are generally recorded by broadband seismometers, which are highly sensitive to ground motion across a wide range of frequencies and record signals at high sample rates (typically 100 times or more per second). This level of detail, however, comes at the cost of generating vast amounts of data. Many seismic networks utilize tens or even hundreds of seismometers at a given time (e.g., Hansen & Schmandt, 2015), making real-time manual inspection of these time series practically infeasible. Previous seismic deployments have also generated extensive legacy datasets that can offer insights into historical volcanic activity and opportunities to further our understanding of volcanic processes. The main challenge is therefore to identify and characterize volcanic earthquakes in a robust and timely manner so as to provide vital clues regarding the state of a volcano and the likelihood or impact of an eruption or hazard, as well as be able to accurately and efficiently process large existing datasets for further analysis within a reasonable timeframe.

Identifying earthquake phase arrivals, particularly the initial primary (P-) and secondary/shear (S-) wave arrivals, forms the basis of most seismic processing tasks (e.g., determining locations, magnitudes and source parameters). Manually identifying these phase arrivals yields greater accuracy and estimates of arrival time uncertainty than automated approaches but is extremely time-consuming. Alternatively, most automated approaches are orders

of magnitude quicker but typically require clear phase arrivals, existing 'templates' of previously catalogued earthquakes (e.g., Gibbons & Ringdal, 2006; Lengliné et al., 2016; Shelly et al., 2007), or pre-processing / feature extraction steps calibrated for a small set of earthquake characteristics (e.g., trigger algorithms based on the ratio of short-term average to long-term average signal amplitude, STA/LTA; Withers et al., 1998). A challenge for application to volcanology is that volcanic earthquakes can exhibit widely varying time-frequency characteristics, often with low amplitudes or obscured phase arrivals, and new phases of unrest can produce previously unseen seismic signals that differ from existing earthquake templates. Furthermore, methods based on existing seismic catalogues are unsuitable for new seismic deployments where a catalogue of events has not been collected.

A recently successful approach for seismic phase arrival detection is the use of supervised deep learning models (e.g., Dokht et al., 2019; Mousavi et al., 2019; Ross et al., 2018b; Woollam et al., 2019; Zhu & Beroza, 2019). These methods are based on convolutional neural networks (CNN), a variant of classical neural networks that employ convolution operations, as opposed to matrix multiplication, in at least part of the model. These operations are employed in 'hidden' convolutional layers that allow the network to learn a large set of filters to extract useful features from the input data and map them to a desired output (e.g., to identify phase arrivals in earthquake waveforms; Fig 1). Typically, multiple convolutional layers are applied in succession and in combination with other operations, such as non-linear 'activation', down-sampling and normalization, to extract complex patterns from the data using a hierarchy of simpler filter kernels. These extracted features can then be fed into a standard fully-connected neural network or other machine learning architecture for classification, segmentation, regression, clustering or inference (e.g., Mousavi et al., 2019; Ross et al., 2018b; van den Ende & Ampuero, 2020). As such, the 'convolutional' part of CNNs act as the model's feature extraction system. With each successive convolutional layer, the extracted features move from lower-level, general signal features (resembling, for example, long/short period wavelets in seismological waveform models; Fig 1A inset) to more task specific, high-level features (Yosinski et al., 2014). The final 'classification' layers of the model map these features to the desired output and can be considered the most task specific part of the model, empirically tuned to the distribution of the training data (Yosinski et al., 2014).

Such an approach gives supervised deep learning models a strong advantage over traditional algorithms that require considerable manual intervention or rely on a small set of manually determined characteristics and simple threshold criteria. In general, however, these models require substantial amounts of labelled data during training to generalize to out-of-sample data (the amount dependent on various factors, such as network architecture, number of network parameters and training hyperparameters; e.g., D'souza et al., 2020; He et al., 2019; Sun et al., 2017). In the case of seismological supervised models, these models can demonstrate impressive levels of generalization to phase arrival detection in other geographic and tectonic settings, if trained with sufficient data (e.g., Mousavi et al., 2020; Tan et al., 2021). However, as with practically any deep learning model, they can also suffer significant loss in performance when faced with data that differs in source or distribution from their training data (e.g., Barbedo, 2018; Zech et al., 2018; Fig 7). As such, the requirement for extensive training sets can place the traditional paradigm of supervised learning (i.e., using a large amount of hand-labelled data to train a single model for a desired domain or problem) out of reach for many real-world applications.

Transfer learning is based on the idea of knowledge transfer from one task to another (Pan & Yang, 2010; Zhuang et al., 2020) and can be a powerful tool when we do not have sufficient labelled data to train a reliable model from scratch, or when existing models perform poorly. At its simplest, the first n convolutional layers and their weights from the feature extraction part of an existing model are copied to the first n layers of a new model for a related or similar task, with the remaining layers either re-initialized with randomized weights or replaced (e.g., Razavian et al., 2014; Yosinski et al., 2014). These tasks need not be near-identical or even superficially related, as long as low-level data characteristics are shared between tasks (e.g., Efremova et al., 2019; Tran et al., 2020; Zamir et al., 2018). The intuition is that generalized knowledge of data structure and properties from one model trained with abundant labelled data (or 'big data') can guide a learning algorithm towards a good solution for a new task with far more limited, or even no, labelled data.

In this paper, we evaluate the utility of inductive transfer learning (i.e., when labelled data are available for both the source and target tasks) for small seismic training sets and produce a

deep learning model that accurately and robustly picks phase arrivals from a deployment at Nabro volcano in Eritrea, a region with little or no prior seismic monitoring. We leverage the knowledge acquired from training a model on millions of seismic waveforms recorded by the Southern California Seismic Network (SCSN), hereby referred to as the GPD model (Generalized seismic Phase Detection; Ross et al., 2018b), and apply it to seismograms from Nabro volcano in Eritrea, for which we have limited hand-labelled data (manual phase arrival picks) from the first couple of months of a 14-month seismic deployment (Goitom, 2017; Hamlyn et al., 2014). The new model task differs from the original GPD model task in that it is modified from one of *classification* (assigning a single class label *P-wave*, *S-wave* or *noise* to an entire 4-second waveform; Fig 1A) to one of *segmentation* (assigning a class label *P-wave*, *S-wave* or *noise* to *each datapoint* within that 4-second waveform; Fig 1B). We achieve this by replacing the fully-connected uppermost layers of the original GPD model with further convolutional layers, creating an all-convolutional model commonly referred to as a U-Net (Ronneberger et al., 2015). We refer to this specific model design as the U-GPD model, utilizing GPD model weights within a U-Net architecture. The new data from Nabro volcano also exhibit differences in instrument calibration and sample rates from the original GPD model training data, as well as differing waveform characteristics between tectonic and volcanic event types (Lahr et al., 1994; Lapins et al., 2020; McNutt & Roman, 2015).

In the following section, we introduce transfer learning and recent applications in seismological deep learning. In Sections 3 and 4, we present our proposed transfer learning method, U-GPD model architecture and seismic data recorded at Nabro volcano. In Section 5, we present a series of model comparisons. We first use common training metrics to demonstrate that transfer learning reduces overfitting and model error, particularly for very small training sets (< 1000 waveforms), when compared with a model reinitialized with randomized weights before training (i.e., trained from scratch with no transfer learning). We then apply these new models to a test dataset of known P-/S-wave arrivals and sections of noise and compare performance with off-the-shelf applications of the base GPD model and another extensively-trained phase-picking model, PhaseNet (Zhu & Beroza, 2019). We find that the U-GPD transfer learning model yields improved phase arrival identification, particularly for S-waves, and false detection rate at Nabro volcano. Altering the model task from classification to segmentation also improves pick time residuals over the base GPD model for these test data. Finally, we apply both our new U-GPD

transfer learning model and the original base GPD model to the full 14-month seismic deployment at Nabro volcano through a sliding window approach. The new U-GPD model identifies more useable S-wave arrivals than the base GPD model, yielding smaller subsequent location errors than even our manual analyst's phase arrival picks. The new model also runs an order of magnitude faster, processing 14 months of data from 7 broadband seismometers in less than 4 hours on a single GPU. Our findings indicate that transfer learning can be extremely useful for volcano seismic monitoring, even with limited computing resources and data. We conclude this paper with a discussion of our findings, methodology and practical considerations of transfer learning in Section 6. All data and code used throughout this paper are made fully and publicly available (see *Data Availability Statement*).

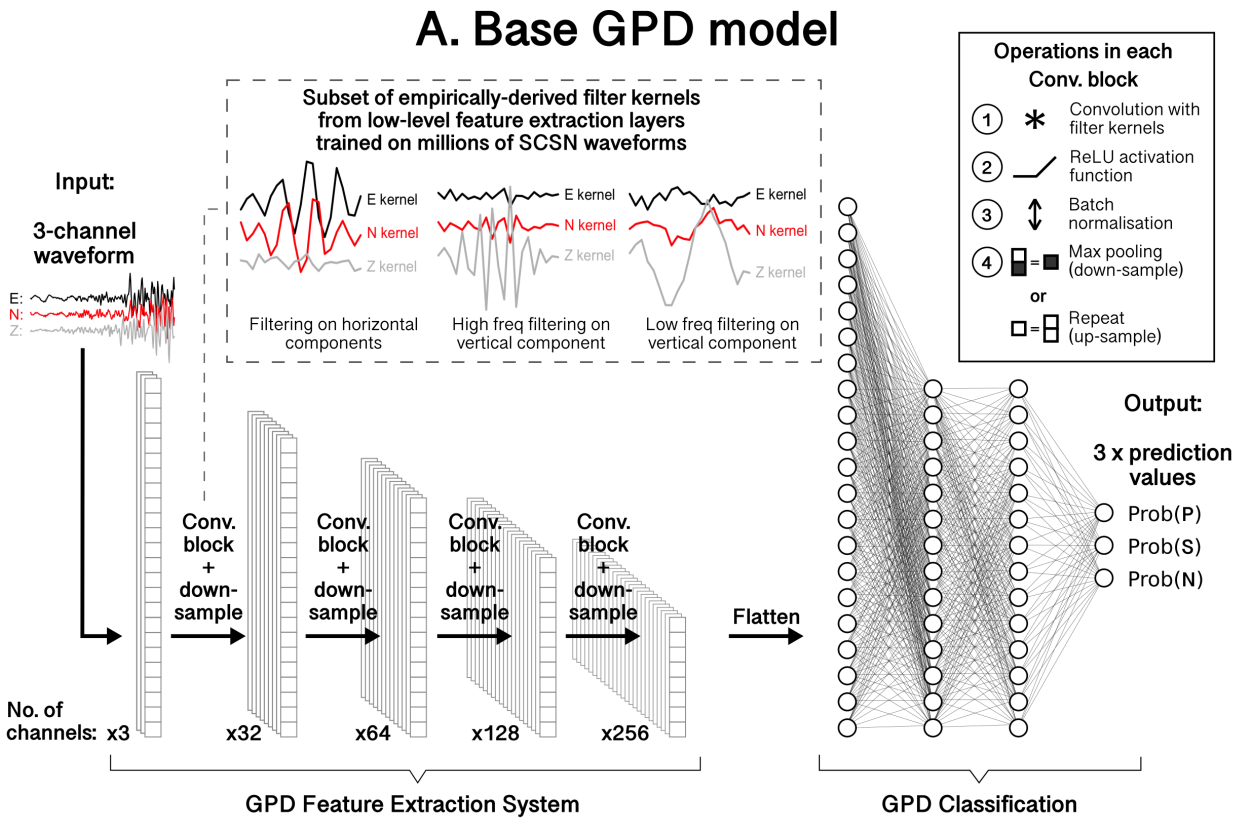
A. Base GPD model
Operations in each Conv. block
1 Convolution with filter kernels
2 ReLU activation function
3 Batch normalisation
4 Max pooling (down-sample)
or
Repeat (up-sample)
Subset of empirically-derived filter kernels from low-level feature extraction layers trained on millions of SCSN waveforms
E kernel
N kernel
Z kernel
Filtering on horizontal components
High freq filtering on vertical component
Low freq filtering on vertical component
Input:
3-channel waveform
E:
N:
Z:
Conv. block + down-sample
Flatten
Output:
3 x prediction values
Prob(P)
Prob(S)
Prob(N)
No. of channels: x3
x32
x64
x128
x256
GPD Feature Extraction System
GPD Classification

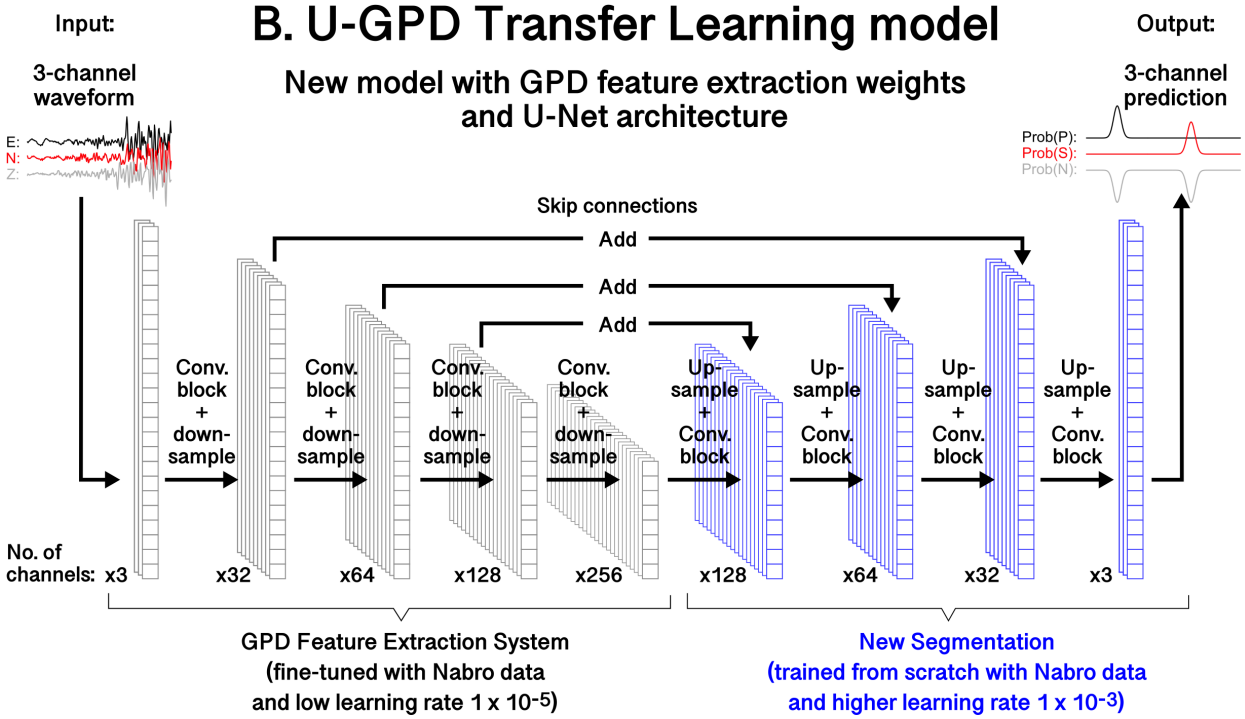
B. U-GPD Transfer Learning model
New model with GPD feature extraction weights and U-Net architecture
Input:
3-channel waveform
E:
N:
Z:
Output:
3-channel prediction
Prob(P):
Prob(S):
Prob(N):
Skip connections
Add
Add
Add
Conv. block + down-sample
Up-sample + Conv. block
No. of channels: x3
x32
x64
x128
x256
x128
x64
x32
x3
GPD Feature Extraction System
(fine-tuned with Nabro data
and low learning rate 1 x 10-5)
New Segmentation
(trained from scratch with Nabro data
and higher learning rate 1 x 10-3)

Figure 1. **A)** Model architecture for Generalized seismic Phase Detection (GPD) CNN model (Ross et al., 2018b). Model can be considered as two parts: a feature extraction system (convolutional layers) and classification part (fully connected layers). GPD model outputs 3 x prediction values (probability of P, S or noise) for an entire 400-sample 3-component waveform (i.e., output dimensions: 1 x 3). Examples of filter kernels (dashed line inset) from lowest convolutional layer that extract generalized seismic waveform features determined through model training on extensive SCSN dataset. These indicate that the GPD model has learnt to extract different features from vertical and horizontal components. **B)** Proposed transfer learning model architecture ("U-GPD"). GPD model feature extraction system is copied to new model and fine-tuned with new Nabro data and low learning rate. Low learning rate ensures that useful features are not 'unlearned'. New convolutional layers replace the GPD classification layers and are trained using new Nabro data and higher learning rate. Model outputs 3 x prediction values for each datapoint in 400-sample 3-component waveform (i.e., output dimensions: 400 x 3).

2 Transfer Learning

There are many approaches to transfer learning (see Pan & Yang, 2010; Zhuang et al., 2020 for comprehensive surveys), including using 'off-the-shelf' feature extraction systems from existing state-of-the-art CNNs (e.g., Maqsood et al., 2019; Razavian et al., 2014), learning domain-invariant or global representations across multiple tasks (e.g., Glorot et al., 2011; Li et al., 2014; Tzeng et al., 2015; Zhuang et al., 2015), applying pre-processing steps to make input data representations more similar between datasets (e.g., Daumé, 2007; Sun et al., 2016) and the use of domain-adversarial models (e.g., Ganin et al., 2016). Here we employ the first of these approaches for P- and S-wave arrival time picking at Nabro volcano, utilizing pre-trained filters from an existing, extensively trained CNN model (the GPD model; Ross et al., 2018b) to train a new model with different output dimension and task type (see *Section 3.1, U-GPD Model Architecture*). Most seismological studies that have employed transfer learning in this way have used pre-trained filters from models designed for non-seismological tasks, such as image recognition. For example, filters trained to recognize photographic images or handwritten characters have been used to detect earthquakes and classify volcano-seismic event types from spectrograms (Huot et al., 2018; Lara et al., 2020; Titos et al., 2020) and interpret seismic facies (Dramsch & Lüthje, 2018).

Some studies have chosen to fine-tune entire seismic deep learning models, essentially updating the models with new data (or equivalently 'pre-training' the models with larger datasets, depending on perspective). El Zini et al. (2020) pre-train an autoencoder with abundant unlabeled data to learn compressed data representations of 2D seismic images. These model weights then serve as a starting point for a model that segments seismic images, with weights fine-tuned using limited labelled training data. This approach was shown to outperform the transfer of weights from image recognition models and training a model from scratch. Bueno et al. (2020) fine-tune a Bayesian neural network (BNN) to improve classification of volcano-seismic event characteristics between datasets and time periods. They show that this approach increases model accuracy and reduces epistemic uncertainty when applied to new volcanic systems or phases of activity. With a similar aim but different approach to the work of this paper, Chai et al. (2020) utilize pre-trained weights from another existing phase arrival detection model, PhaseNet (Zhu & Beroza, 2019), to pick phase arrivals from hydraulic fracturing experiments. They use the entirety of the PhaseNet model and its pre-trained weights as a starting point for training and then fine-tune all model weights equally using just 3,500 seismograms. They present improved results over the original PhaseNet model, which was trained using 700,000 seismograms of regional Californian seismicity, when applied to higher sample rate data (100 kHz) from a very different setting (i.e., hydraulic fracturing). Whilst these studies show that fine-tuning entire models can be an effective strategy, poor hyperparameter choices (model learning rate, number of training epochs, etc.) can inadvertently retrain the model (also known as 'catastrophic forgetting'; e.g., Kirkpatrick et al., 2017) or lead to settling on a non-global minimum within the parameter space, reopening the potential for overfitting when the number of model parameters is large and the training dataset is small (El Zini et al., 2020; Yosinski et al., 2014). The work in this paper differs from that of Chai et al. (2020) in that only the weights from the feature extraction part (i.e., the first 'half') of the GPD model are transferred to our new U-GPD model. These weights are fine-tuned using a much lower learning rate (weight update step size) to retain useful learned knowledge from the original model but optimize cohesion with the rest of the new model, which is redesigned to reduce the total number of trainable parameters, among other optimizations (see Section 3.1, Model Architecture), and initialized with randomized weights (Fig 1).

3 Proposed Model

3.1 U-GPD Model Architecture

As outlined briefly above, we utilize pre-trained parameters from the convolutional layers of the GPD model as a starting point for our U-GPD transfer learning model. The original GPD model was trained using 4.5 million hand-labelled seismograms (1.5 million of each class *P*, *S* and *noise*) recorded by the Southern California Seismic Network (SCSN) between the years 2000 and 2017. These training data were all 400-sample (4 sec) 3-component waveforms, high-pass filtered above 2 Hz and (re)sampled at 100 Hz. All events had epicentral distances less than 100 km and magnitudes between -0.81 and 5.7 M (various magnitude scales). The GPD model was chosen as a base for our transfer learning model as these data characteristics (magnitude range, sample rate and event distances) are comparable to those observed and recorded by volcano observatories. Furthermore, the short input length of 4 seconds (400 samples at 100 Hz sample frequency) means there is less chance of erroneously labelling or missing relatively small magnitude or overlapping phase arrivals. Finally, the GPD model's 'sequential' architecture, with each layer being solely connected to the layers directly before and after, also means the model is more interpretable and makes it easier to isolate its feature extraction system.

During model training, we fine-tune these pre-trained parameters using a very small learning rate (1×10^{-5}), rather than keep them fixed (e.g., Yosinski et al., 2014). Learning rate effectively controls how much model weights can change and a small learning rate will keep adjustments to the pre-trained GPD feature extraction weights small. The aim of this fine-tuning step is to modify any highly specific features from the source domain (particularly in the higher-level feature extraction layers) and overcome optimization difficulties arising from splitting the GPD convolutional layers from co-adapted classification layers (Yosinski et al., 2014), without unlearning the important generalized waveform features we wish to exploit.

We then replace the GPD model's fully-connected layers (i.e., the task-specific classification part of the model) with further convolutional layers and up-sampling operations, combined with ReLU activation function (Nair & Hinton, 2010) and batch normalization (Ioffe &

Szegedy, 2015), to produce a model output with the same dimensions as model input (400 samples x 3 channels; Fig 1B). Each of the three output channels represents the model's prediction (or 'probability') of a P-wave arrival, S-wave arrival or neither (hereby referred to as *noise*), respectively, at each datapoint in the waveform. This all-convolutional approach has been adopted by other phase arrival picking models (e.g., Woollam et al., 2019; Zhu & Beroza, 2019) and has several distinct advantages when applied to seismic phase arrival detection: i) it provides less ambiguous labelling of phase arrivals when compared to the original GPD model's approach of assigning a single class prediction (*P*, *S* or *noise*) to an entire 400-sample 3-channel waveform; ii) convolutional layers tend to have fewer parameters than fully connected neural network layers so less training data is required to avoid overfitting; iii) by producing a model with input and output traces of same dimension, we require less overlap when applied as a rolling window method, producing a model that runs orders of magnitude faster on continuous sections of data.

The new convolutional layers are initialized with completely randomized weights and trained with a higher learning rate (1×10^{-3}) than the pre-trained GPD weights. A higher learning rate effectively allows the randomized weights in the new model layers to be adjusted much more than the pre-trained GPD weights. The learning rates used for each part of the model were determined through experimentation, insight from previous works (e.g., Ross et al., 2018a, 2018b), and on the basis that the learning rate for fine-tuning pre-trained weights should be orders of magnitude lower than that used for tuning randomized weights (e.g., Yosinki et al., 2014). We note that there are more formal strategies (e.g., grid/random search, Bayesian optimization, bandit strategies, gradient reversal; Bergstra & Bengio, 2012; Feurer et al., 2015; Klein et al., 2016; Maclaurin et al., 2015; Snoek et al., 2015) for determining optimal model hyperparameters. Such strategies, however, add significant computational cost as they generally require repeatedly training models with differing hyperparameter choices, producing a much greater search space. The aim in this study is not to present the absolute best possible model architecture and set of hyperparameters specific to this deployment at Nabro (as these choices will likely be specific to application and training set size) but to illustrate how existing models can be tailored to new datasets to improve performance in those settings. Furthermore, it would prove more difficult to attribute any observed improvements to the use of transfer learning and U-Net architecture, as opposed to the hyperparameter optimization strategy. We do, however, implement two further

hyperparameter choices that were found to improve performance. First, we use dilated filter kernels in the new convolutional layers (e.g., van den Oord et al., 2016; Yu & Koltun, 2016) to increase the size of the model's receptive field (or 'field of view') and aggregate multi-scale context. Second, the new layers are subjected to spatial dropout (Tompson et al., 2015), where 30% of the feature maps (output of filter operations) in each convolutional layer are effectively dropped (set to zero) at the start of each training epoch. This step promotes independence between the features the model extracts and prevents overfitting (Tompson et al., 2015). Precise details of U-GPD model dimensions and hyperparameters are provided in *Supplementary Materials* (Fig S1).

The overall network architecture outlined above is sometimes referred to as a U-Net (Ronneberger et al., 2015). With each step through the network, the input data are progressively downsampled with an increasing number of features extracted, creating a contracting network path that is forced to sacrifice detail and learn a more compressed, general representation of the input waveform to discriminate between classes (*P*, *S* or *noise*). The model then follows a symmetrically expanding path, where the data are progressively upsampled and the number of features reduced, to regain precise temporal or spatial detail and return an output with equal dimension to the model input (Ronneberger et al., 2015). Skip connections (addition operators), which act as direct, one-way pathways between layers in the contracting and expanding sides of the model (Fig 1B), are used to retain precise waveform details that may be lost through this contraction/expansion process and have been shown to greatly improve the likelihood of model parameters settling on the global minimum during training (Li et al., 2017).

3.2 Phase Arrival Labels and Model Hyperparameters

Each 3-component waveform in our training dataset has a corresponding 3-channel 'mask' that provides a ground truth label (*P*, *S* or *noise*) for each waveform datapoint. During training, the model aims to minimize the difference between its predictions and these ground truth labels. Labels are presented as binary values (0's or 1's), with P-wave arrivals indicated by a +/- 0.14 sec boxcar function, centered on the manually picked P-wave arrival time, and S-wave arrivals indicated by +/- 0.19 sec boxcar function, also centered on the manually picked S-wave arrival

time. These boxcar widths provide a good balance between phase arrival detection rate and arrival time precision and compensate for human error in the ground truth labels. Previous studies have used Gaussian-style probability masks, with values ranging between 0 and 1, for labelling phase arrivals (e.g., Woollam et al., 2019; Zhu & Beroza, 2019). We find that label accuracy on our test data (e.g., Figs 5, 6 and 7) and event location error distributions from the full deployment (e.g., Fig 10C & D) are near-identical when using either approach but training with boxcar masks produces a model that detects ~ 10% more events when run over continuous data.

As with the original GPD model, our new U-GPD model was trained using a categorical cross entropy loss function (Text S7) and the Adam optimization algorithm (Kingma & Ba, 2014). The model weights that produced lowest loss value on the validation dataset during training were selected as our final model weights. Other loss functions that address the imbalance between arrival and noise labels (as the majority of labels in any given waveform are not a phase arrival), such as a focal loss function that effectively adds weighting parameters to cross entropy loss (Lin et al., 2017), were trialed but yielded no improvement in model performance.

4 Data

Nabro volcano is one of two calderas that form the Bidu Volcanic Massif on the Eritrea-Ethiopia international border (Fig 2). Located in the Afar region at the northern end of the Main Ethiopian Rift, it erupted unexpectedly for the first time in recorded history on 12th June, 2011, disrupting continental aviation and initiating a significant humanitarian crisis (Bojanowski, 2011; Donovan et al., 2018; Goitom et al., 2015). At the time, there were no seismic or other monitoring networks operating in Eritrea but earthquakes were felt around the volcano several hours and days prior to eruption, prompting evacuation (Goitom et al., 2015). This seismicity is the first of note in global catalogues for the region (Goitom et al., 2015). Despite this fortuitous warning, at least seven people were tragically killed and about 12,000 were displaced (Bojanowski, 2011; Goitom et al., 2015; Hamlyn et al., 2014). The eruption is particularly notable for the vast amount of SO_2 emitted into the atmosphere, one of the largest eruptive SO_2 masses globally since the eruption of Mount Pinatubo in 1991 (Fromm et al., 2014; Goitom et al., 2015; Theys et al., 2013), and the

comparative rarity of recorded historical eruptions in the region (Goitom et al., 2015; Hamlyn et al., 2014).

In August, 2011, approximately two months after the eruption began, eight 3-component broadband seismometers (5 x Guralp CMG-6T, 3 x Guralp CMG-40T; Fig 2) were deployed around the volcano to monitor ongoing activity (Hamlyn et al., 2014; Hammond et al., 2011). These stations remained operational for 14 months until October, 2012. The first two months of data were collected at a sample rate of 100 Hz before dataloggers were switched to a sample rate of 50 Hz for the remainder of the deployment to maximize data recovery while minimizing service runs. Data from the full deployment occupies 70 GB of disk space (miniSEED format). Manual phase arrival picking conducted on the first four months of data (2011-08-30 to 2011-12-31; Goitom, 2017; Hamlyn et al., 2014) identified a total of 2926 events, from which the first 35 days of data (all 100 Hz sample rate) were quality checked and used for training and validating our transfer learning model. Five subsequent days of data (2 x 100 Hz days, 3 x 50 Hz days) were selected and quality checked to serve as test data. The reason to exclude 50 Hz data from model training is to emulate data availability in the early stages of this seismic deployment and demonstrate that changes in sample rate can be overcome without compiling new training datasets through a process known as data augmentation. The raw data for all datasets (training, validation and testing) were self-normalized, with linear trend removed, and left unfiltered.

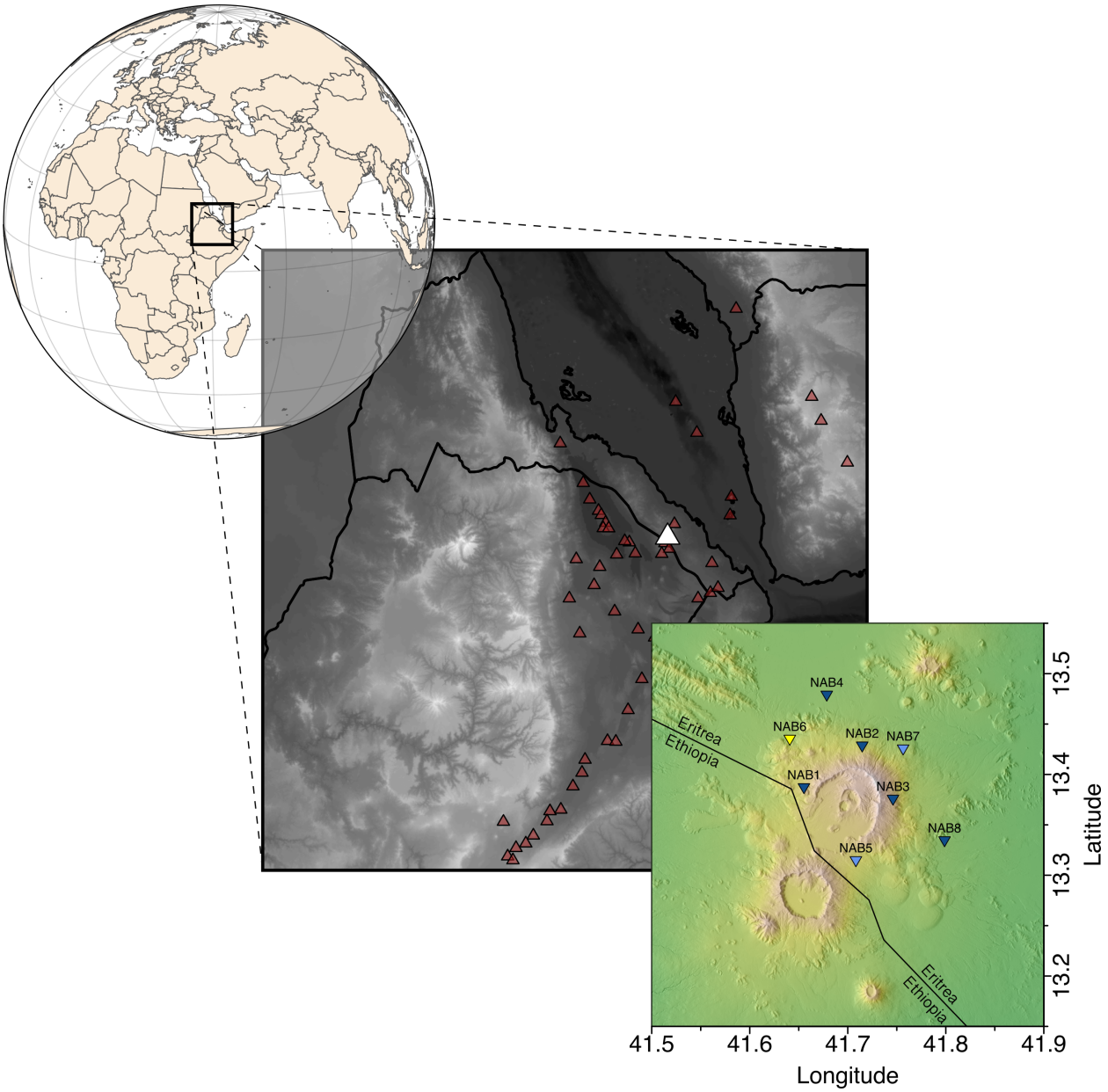

Figure 2. Regional topographic map (90 m CGIAR Shuttle Radar Topography Mission and GEBCO bathymetry model, grey-scale map center) and seismic deployment (30 m ALOS Digital Surface Model, color map bottom right) around Nabro volcano. Red triangles (center map) indicate Holocene volcanoes (Global Volcanism Program, 2013) with Nabro volcano highlighted in white. Inverted blue triangles (bottom right map) indicate operational broadband seismic stations deployed around Nabro volcano from August 2011 to October 2012 (station NAB6, inverted yellow triangle, was flooded shortly after deployment and not operational). Training and validation data were taken from dark blue stations only (NAB1, NAB2, NAB3, NAB4 and NAB8).

A total of 2921 waveforms with labelled P- and S-wave arrivals from 978 events (2011-08-30 to 2011-10-03) and five stations were used as training and validation data (only five stations were consistently operational during this time; dark blue stations in Fig 2 bottom right map). Training and validation data were grouped and divided so that no event appeared in both datasets to avoid data leakage (the model being trained on event data that also appears in validation or testing). 857 events (2498 waveforms) were used for model training and 121 events (423 waveforms) were used for model validation, a training-validation split of approximately 85%-15%. 624 sections of noise (20 secs length) were manually identified across all five stations (2011-08-31 to 2011-09-27), with 500 sections (2500 waveforms) and 85 sections (425 waveforms) used for model training and validation, respectively. Two noise waveforms were randomly dropped from each dataset so that the training and validation noise data comprise 2498 and 423 waveforms, respectively, to match the number of event waveforms.

A separate test dataset of 400 event waveforms with labelled P- and S-wave arrivals (132 events) and 400 noise waveforms (80 sections of noise) was also produced for subsequent model testing. These data come from a different time period than those used for training and validation data, with 200 waveforms from a period where data were recorded at 100 Hz sample rate (2011-10-04 and 2011-10-05) and 200 waveforms from a period with 50 Hz sample rate (2011-10-14, 2011-10-15 and 2011-11-27) for each category. All training, validation and test data were manually identified and quality checked.

The success of U-Net architectures relies on an effective data augmentation strategy when working with smaller datasets (Ronneberger et al., 2015). This allows the network to learn invariance to certain changes in input signal without them needing to appear in the annotated dataset. Here we outline a data augmentation strategy that improves performance of our U-GPD transfer learning model (Fig S2). First, as all stations were switched from 100 Hz sample frequency to 50 Hz sample frequency part way through the seismic deployment, we randomly select subsets of the training data (all originally sampled at 100 Hz) to be decimated to 50 Hz sample frequency throughout training. Each training sample (i.e., each 3-component waveform) has a probability of 0.5 of being selected for decimation before each training epoch, with an anti-aliasing, low-pass

finite impulse response (FIR) filter applied and linear phase shift removed. Second, we randomly time-shift our P- and S-wave arrivals relative to the model input 'window', so that our waveforms differ slightly from epoch to epoch and the model must learn signal features that indicate arrivals rather than where they occur within the input window (i.e., arrivals don't need to occur in the center of the window for the model to detect them). With our noise data, a random 400-sample window is chosen at each training epoch from our 20-second noise sections, introducing more waveform variety between training epochs.

All data processing and model training/testing were performed in Python using the ObsPy (Beyreuther et al., 2010; Krischer et al., 2015; Megies et al., 2011), TensorFlow (Abadi et al., 2015; https://tensorflow.org) and Keras (Chollet et al., 2015; https://keras.io) libraries.

5 Results

5.1 Training Metrics (Transfer Learning vs No Transfer Learning)

To examine the impact of transfer learning and determine how much training data is required to produce an effective model, we use varying sized subsets of the training data throughout model training (i.e., 250, 500, 750, …, 2000, 2250 and 2498 training samples). Figure 3 compares how model loss (measure of distance between model predictions and ground truth labels) on training and validation data evolves throughout training between our transfer learning model and the same model with completely re-initialized weights (i.e., with no transfer learning) for our smallest and largest subsets of training data (250 and 2498 training samples, respectively). The learning rate is set to be equal (1×10^{-3}) across the whole re-initialized model as we are no longer fine-tuning existing knowledge. All other hyperparameters, including dropout rate, are kept the same. The models trained without transfer learning (Fig 3B and D) show a much greater degree of overfitting: the model loss on the training data continues to decrease with more training while the loss on validation data (data that the model does not use during training) hits an inflection point and starts increasing, reflecting that the model is 'memorizing' the precise features of the training data at the cost of generalization (Shorten & Khoshgoftaar, 2019). By contrast, the validation loss continues to decrease for the models trained with transfer learning (Fig 3A and C). Furthermore,

461 the minimum validation loss achieved by the transfer learning models for each training dataset size
462 is lower than when transfer learning is not employed (Fig 3 horizontal dashed lines). Such
463 diagnostics indicate that transfer learning is successfully preventing overfitting to the training data
464 and will likely produce a model that generalizes better to non-training data (Shorten &
465 Khoshgoftaar, 2019). The greatly improved performance on validation data using the smallest
466 subset of training data (Fig 3A and B) shows that transfer learning is particularly useful for
467 reducing overfitting and model loss when training data are very limited, but this advantage is
468 progressively diminished with increasing training dataset size (Figs 3 and 4).
469

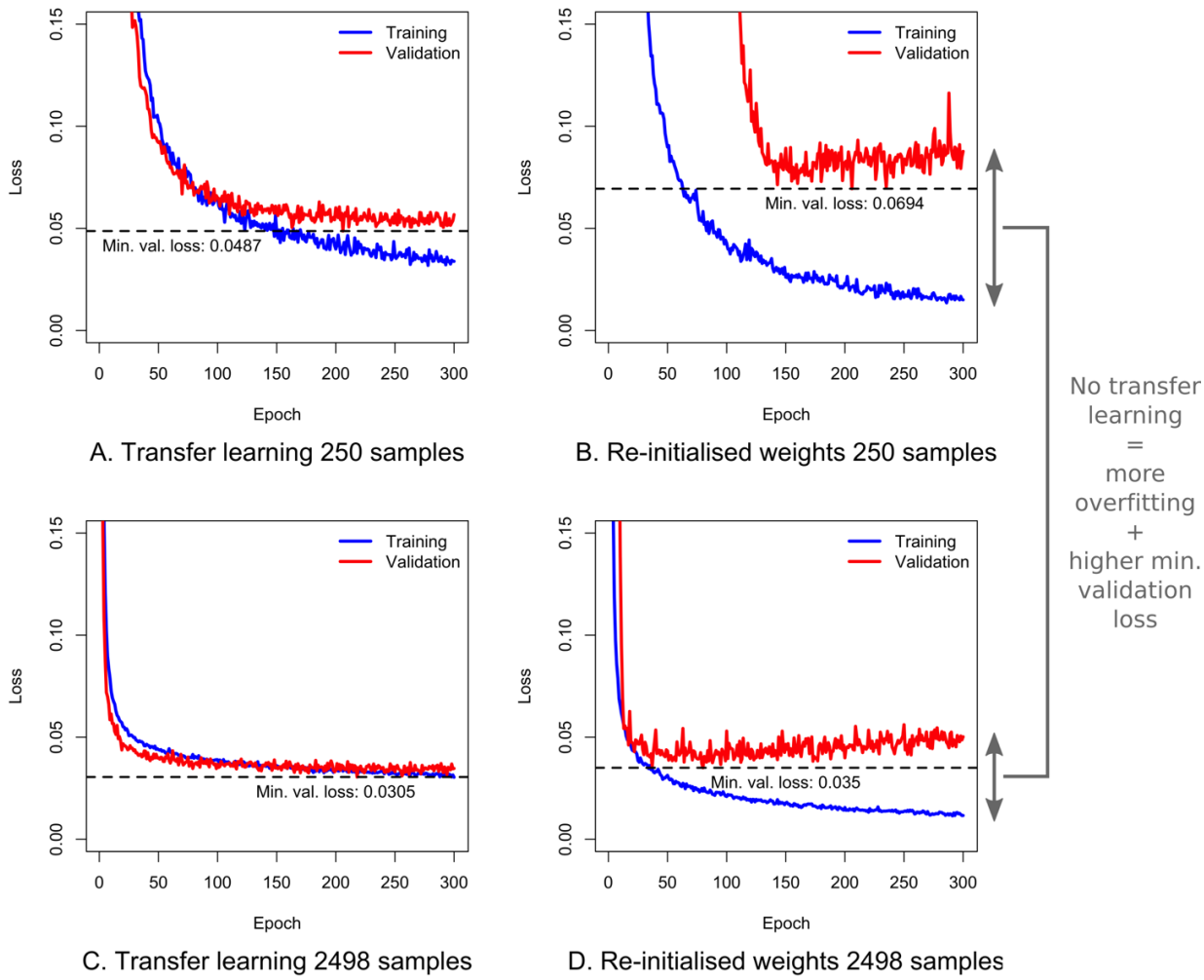

470
471
472 **Figure 3.** Model loss vs. training epoch number. **A)** Transfer learning model and 250 training
473 samples of each class (P, S or neither). **B)** Model trained without transfer learning (i.e., initially

474 randomized weights) and 250 training samples of each class. **C)** Transfer learning model and full
475 training dataset (2498 training samples of each class). **D)** Model trained without transfer learning
476 (i.e., initially randomized weights) and full training dataset. Blue curve shows model loss for
477 training data, red curve shows model loss for validation data (not seen during training). A lower
478 model loss on training data (blue) than validation data (red) means the model shows signs of
479 overfitting. The degree of overfitting (gap between blue and red curves) is much greater for the
480 models without transfer learning (**B** and **D**) with validation loss hitting an inflection point then
481 increasing whilst training loss continues to decrease. The transfer learning models also achieve a
482 smaller minimum validation loss (horizontal dashed line) for each training set size.
483
484 Figure 4 shows the highest model accuracy (the proportion of labels the model classifies
485 correctly) and lowest model loss achieved by our transfer learning and re-initialized models on
486 validation data when trained using each subset size of training data. The transfer learning model
487 achieves lower model loss regardless of training dataset size (Fig 4B). As training dataset size
488 increases, the difference between the lowest loss achieved by the two models (gap between red
489 circles and red triangles, Fig 4B) decreases and the advantages of transfer learning diminish.
490 Generally, loss is considered a more robust metric than accuracy for model performance on future
491 data as it measures the distance between model predictions and ground truth labels, whereas
492 accuracy simply measures a binary true/false score. However, accuracy still provides useful
493 information regarding model performance. In particular, the transfer learning model shows a stable
494 relationship between maximizing model accuracy and minimizing model loss (gap between black
495 and red circles is very small for all training subset sizes), where the training strategy of minimizing
496 model loss appears to achieve the same goal as maximizing model accuracy, again a sign of
497 reduced overfitting. The re-initialized model (black and red triangles), on the other hand, shows a
498 much less stable relationship in this regard, with diverging training scores (Fig 4) indicating that
499 high model accuracy comes at the cost of higher model loss and low model loss comes at the cost
500 of lower model accuracy for these small training set sizes when transfer learning is not employed.
501 The increased model loss for model weights with highest model accuracy (black triangles) also
502 suggests that the model has become overconfident in its predictions (it has large errors on the small
503 proportion of labels it gets wrong) and is therefore likely to perform worse on out-of-distribution

data, with more false or missed phase arrival detections (e.g., a phase arrival being labelled as noise with high model confidence, or vice versa).

Model performance between the two approaches (transfer learning vs re-initialization) converges as training set size increases, indicating that the need for transfer learning decreases with increased training set size, as expected. In fact, model performance with transfer learning appears to plateau, or possibly even degrade, at training subset sizes of more than 1500 samples. This suggests that, with enough training data, transfer learning could potentially inhibit the model's ability to learn useful features in the new data that are absent in the original GPD training data. This apparent variance in performance may also simply be a result of the stochasticity arising from training using randomized weights in the new part of our transfer learning model.

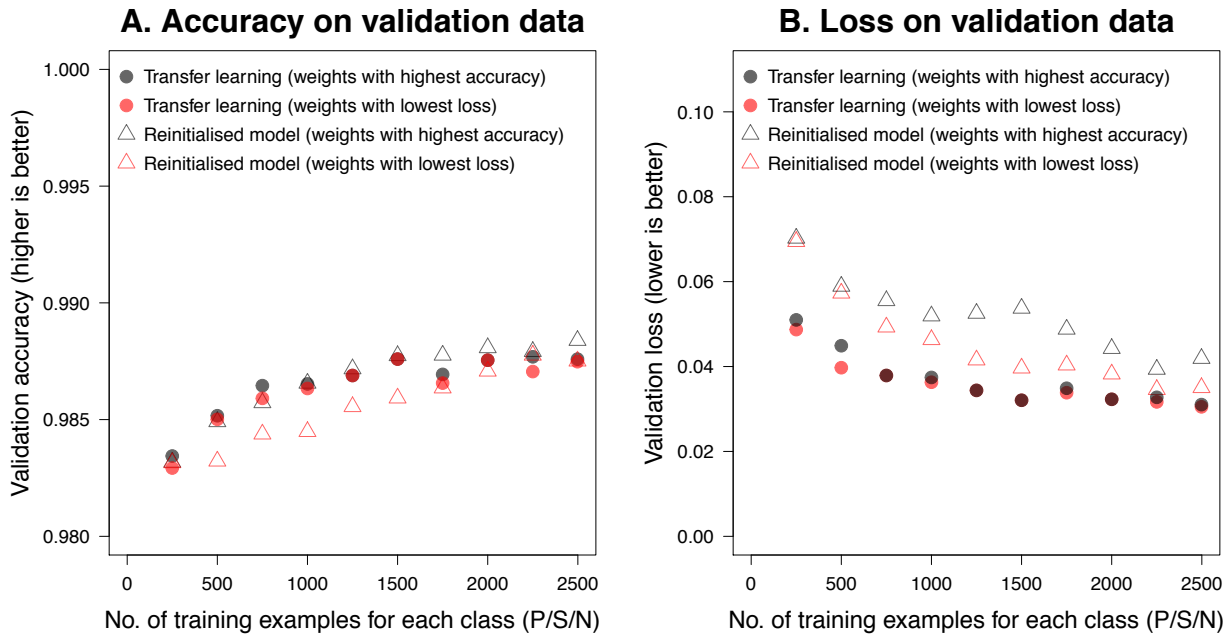

Figure 4. Model accuracy (**A**) and loss (**B**) for various subsets of training data. Open red circles are transfer learning model weights from epoch that achieves lowest validation loss (e.g., dashed horizontal lines in Fig 3), open black circles are transfer learning model weights from epoch that achieves highest validation accuracy, solid red triangles are re-initialized model (no transfer learning) weights from epoch that achieves lowest validation loss, and solid black triangles are re-initialized model weights from epoch that achieves highest validation accuracy.

524

525 **5.2 Test Dataset (Known Arrival Times)**

526

527 Following model training, we test the above models (i.e., new model with and without
528 transfer learning) and two baseline models (GPD and PhaseNet) using the test dataset outlined in
529 Section 4. We examine the proportion of correct class predictions (Fig 5) and the residuals between
530 model and manually determined phase arrival pick times (Fig 6). Due to differences in model task
531 types (classification vs segmentation), we apply all models as sliding windows over 1000-sample
532 waveforms (note that the PhaseNet model takes a 3000-sample waveform as input so we examine
533 only the middle 1000 samples for this model). To account for human picking error in collating our
534 test set, we define a true positive for each phase arrival type (P or S) as the model prediction
535 exceeding a given threshold value for that arrival type within 0.5 secs of the manually determined
536 arrival, such that predicted arrival times very close to the manually determined arrival time are
537 considered accurate. A true positive for sections of noise is defined as no phase arrival prediction
538 exceeding a given threshold value at any point within that section of data. The test data are pre-
539 processed as per the training data for each model (i.e., GPD model tested on 2 Hz high-pass filtered
540 data and all other models, including PhaseNet, tested on raw data; all detrended and self-
541 normalized).

542

543 The GPD model is tested using four different threshold values (Fig 5A – D) as this value
544 strongly controls the number of false or missed phase arrival detections generated by this model.
545 When the threshold is set to be whichever class label (P, S or N) has the highest predicted value
546 for a given waveform, nearly all P- and S-wave arrivals are detected by the GPD model (99.75 %
547 and 95 % detection rate, respectively; Fig 5A). However, this threshold criterion makes the GPD
548 model extremely prone to false phase arrival detections in sections of noise, with 44 % of 1000-
549 sample noise waveforms in our test dataset containing at least one false phase arrival detection
550 (Fig 5A, bottom right square) and many of our 1000-sample event waveforms containing multiple
551 phase arrival triggers (e.g., Fig 7B & E). When this threshold criterion is applied to continuous
552 sections of data from Nabro, the number of false phase arrival detections overwhelmingly
553 outweighs the number of true phase arrival detections and becomes unmanageable in terms of

554 correctly associating phases, identifying true events and processing the data within computational
555 memory constraints.
556
557 One way to lower the number of false phase arrival detections is to use a higher threshold
558 value for P- and S-wave predictions. Figure 5B shows the GPD model's performance on our test
559 data using a 0.9 threshold value (i.e., a P or S prediction 'probability' must exceed 0.9 to be
560 included). The number of false detections in sections of noise is greatly reduced (down from 44 %
561 of waveforms to 10 % of waveforms) but at the cost of reduced true phase arrival detections (~
562 95% and ~82% of P- and S-wave arrivals, respectively). Part of this performance dip is
563 undoubtedly due to the difference in sample rates between one half of the test data (50 Hz) and the
564 GPD model's training data (all 100 Hz). When the threshold value is increased further (i.e., P or S
565 prediction must exceed 0.95 or 0.99; Fig 5C and D), the GPD model yields even fewer false phase
566 arrival detections in noise sections but at the cost of fewer P- and S-wave arrivals.
567
568 Figure 5E shows the performance of the PhaseNet model on our test dataset. This model is
569 included as it adopts the same U-Net segmentation approach as our new model and is trained on
570 data from a variety of instrument types, although the training data is still exclusively from
571 California. The PhaseNet model is much less prone to false phase arrival detections than the GPD
572 model (Fig 5E, bottom right square); as such, a much lower threshold value (0.4) can be used to
573 maximize the number of true phase arrival detections. This model accurately identifies ~ 89% and
574 ~ 83 % of P- and S-wave arrivals in our test dataset, which is better than the GPD model with a
575 threshold value that achieves a similar false detection rate (e.g., Fig 5D), but detects fewer phase
576 arrivals than our transfer learning and reinitialized models trained with Nabro data (Fig 5F – I).
577

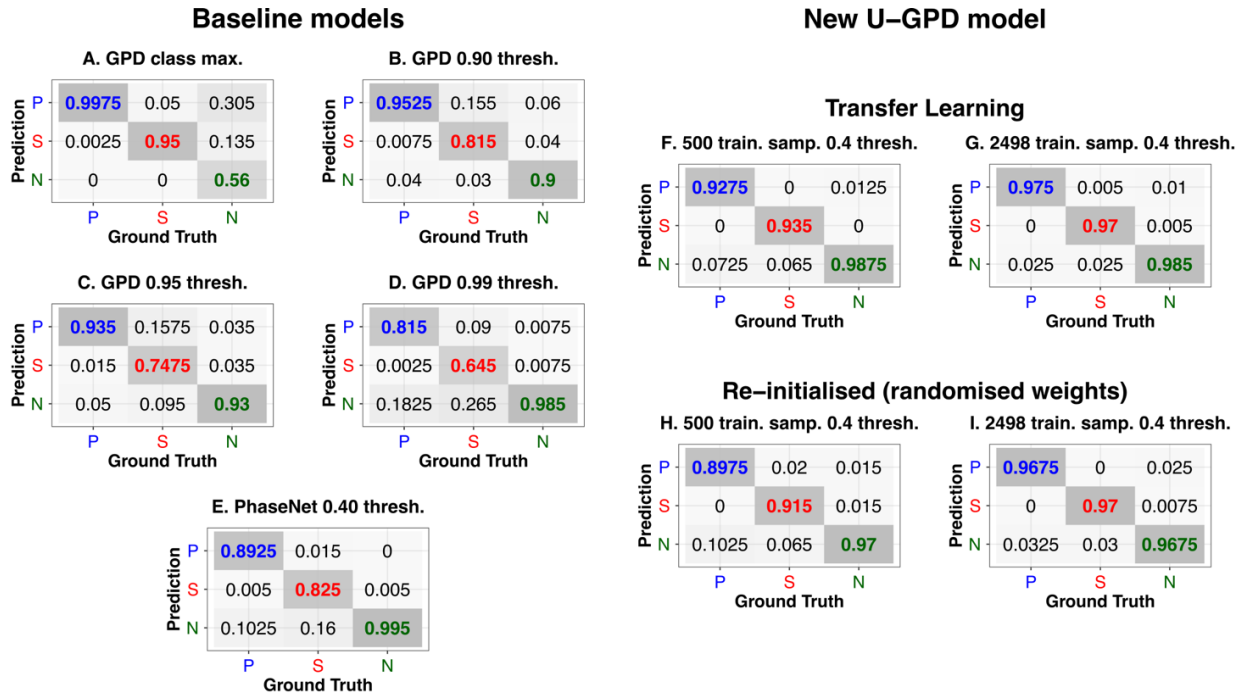

Figure 5. Confusion matrices for base GPD model (**A – D**), PhaseNet model (**E**), U-GPD transfer learning model (**F**, 500 training samples, and **G**, 2498 training samples) and re-initialized model (**H**, 500 training samples, and **I**, 2498 training samples). Values in matrices are proportion of ground truth phase arrivals (test set) assigned by each model to a given class (values of 1 along diagonal from top left to bottom right means all phase arrivals and sections of noise correctly identified).

When trained using a subset of just 500 training samples for each class (P/S/N) and evaluated using a prediction threshold value of 0.4, the transfer learning approach correctly detects ~ 93% and ~94% of P- and S-wave arrivals with very few false phase arrival detections in sections of noise (~ 1 %; Fig 5F), a clear improvement over our model trained with re-initialized weights and the same training subset (Fig 5H). When our full training dataset is used (2498 samples for each class), model performance converges between transfer learning (Fig 5G) and re-initialization (Fig 5I), with a similar number of correctly identified phase arrivals and false detections in noise, although the transfer learning model still performs marginally better, particularly on sections of noise. In essence, the transfer learning model strikes a better balance between high phase arrival detection rate (~ 97 – 98% for each phase arrival type; Fig 5G, top left and center squares) and low

597 false detection rates in sections of noise (~ 1%; Fig 5G, bottom right square) on our test data from
598 Nabro volcano than any of the existing baseline models (Fig 5A – E) or training a model from
599 scratch (Fig 5I).
600
601 Figure 6 shows the residuals for each model between their predicted phase arrival times
602 and the original manual pick times for these test waveforms. Predicted phase arrival times were
603 determined using a simple trigger algorithm (e.g., Withers et al., 1998) on each model's probability
604 time series with the time series index that yields maximum predicted value chosen as the pick time
605 for a given phase arrival type (Fig 7). The models that employ semantic segmentation (i.e.,
606 PhaseNet, our U-GPD transfer learning model and our re-initialized model; Fig 6B – F) show
607 comparable pick time precision (root mean square deviation [RMSD] of 0.036, 0.038 and 0.044
608 seconds, respectively, for each model's P-wave predictions and RMSD of 0.053, 0.053 and 0.065
609 seconds, respectively, for each model's S-wave predictions). The GPD model (Fig 6A), by
610 comparison, has a more diffuse range of phase arrival pick times (RMSD of 0.217 seconds for P-
611 waves and 0.188 seconds for S-waves), with some model picks made more than 1 second before
612 or after the manually determined arrival time. This is almost certainly a result of its more
613 ambiguous class labelling (Fig 1) and the broad phase arrival probability peaks it generates (Fig
614 7).
615

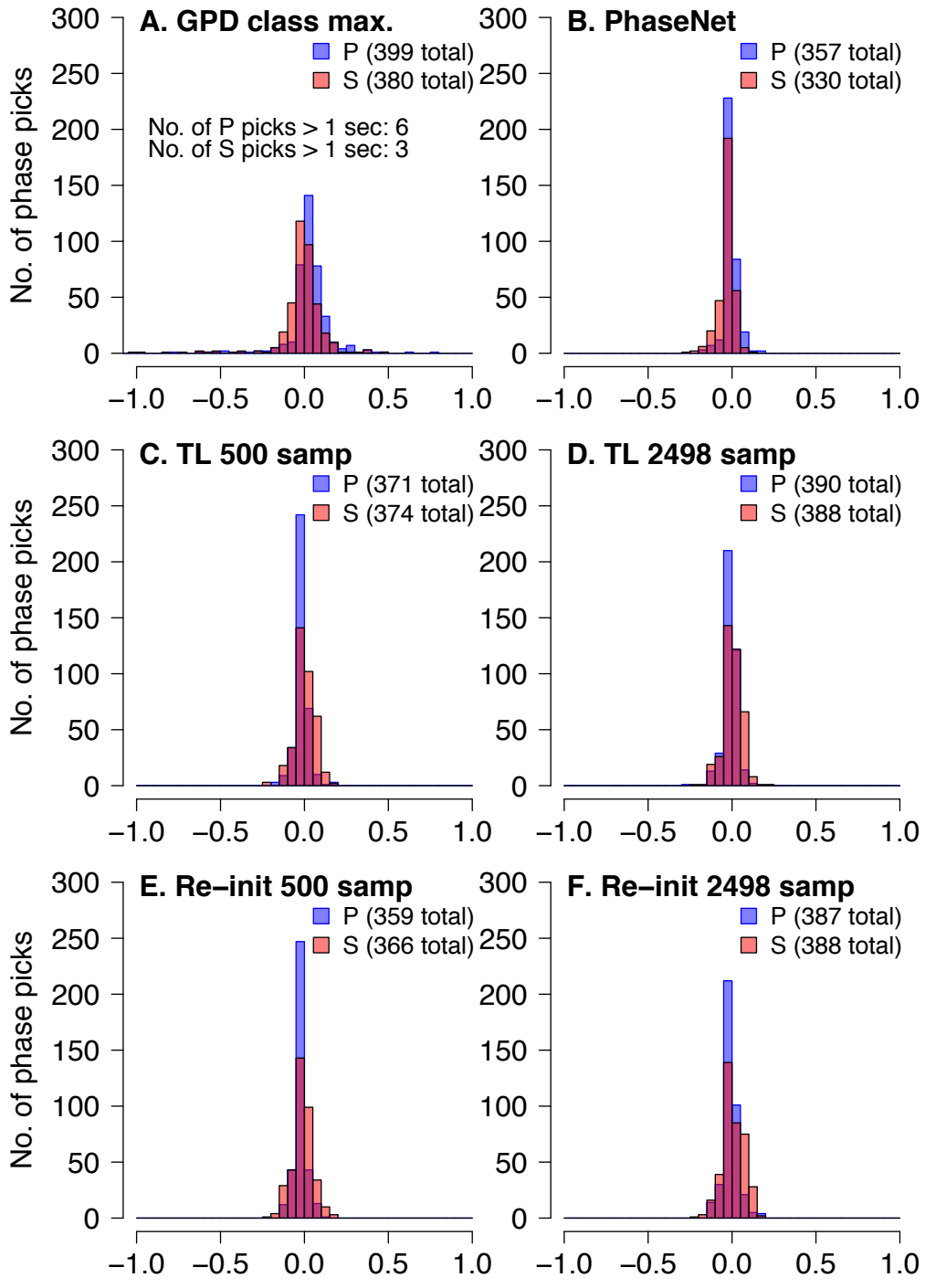

Figure 6. Model phase pick residuals vs. manual phase picks for base GPD model (**A**), PhaseNet model (**B**), U-GPD transfer learning model (**C**, 500 training samples, and **D**, 2498 training

620 samples), and reinitialized model (**E**, 500 training samples, and **F**, 2498 training samples). The
621 models based on semantic segmentation (**B – F**) yield smaller phase pick residuals.
622
623 Figure 7 shows three example waveforms from the test set with corresponding model
624 predictions for the U-GPD transfer learning, GPD and PhaseNet models. These waveforms were
625 chosen as they have low SNR phase arrivals. Prediction labels for the U-GPD model resemble the
626 boxcar labels of the training set (Fig 7A, D & G), whereas prediction labels produced by the
627 PhaseNet model resemble the model's truncated Gaussian-style training labels (Fig 7C, F & I).
628 Despite these boxcar shapes, the U-GPD model's maximum predicted value for each phase arrival
629 consistently and accurately picks both P- and S-wave arrivals (Fig 7A, D & G). On the other hand,
630 the base GPD model's prediction labels are considerably broader and noisier (Fig 7B, E & H). The
631 U-GPD model appears to have benefitted from retraining using Nabro-specific data, as it performs
632 much better than the existing models on these challenging waveforms.
633

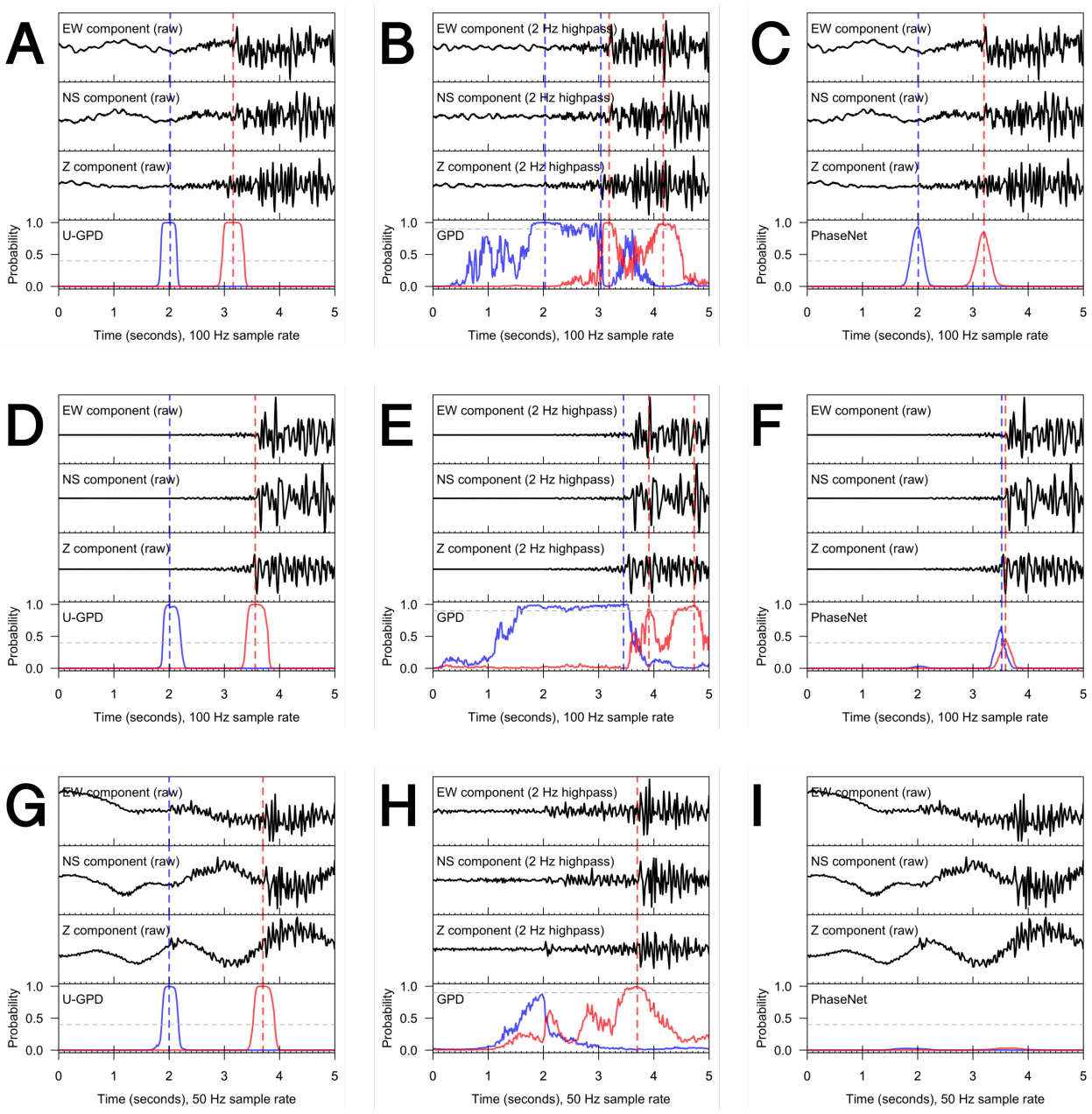

Figure 7. Three example waveforms from our test set. Phase arrival prediction trigger thresholds (horizontal dashed lines) are 0.4, 0.9 and 0.4 for U-GPD (left), GPD (center) and PhaseNet (right), respectively. (**A** – **C**), Test waveform with substantial high frequency background noise. All models accurately detect P- and S-wave arrivals but GPD model makes multiple phase detections. (**D** – **F**), Test waveform with low amplitude P-wave arrival. Existing GPD and PhaseNet models incorrectly label S-wave arrival as close combination of P-wave arrival and S-wave arrival. U-GPD transfer learning model correctly detects both P- and S-wave arrivals. (**G** – **I**), Test waveform with substantial low frequency background noise. P-wave arrival prediction is below trigger

thresholds for both GPD and PhaseNet models, although GPD model accurately detects S-wave arrival. U-GPD transfer learning model correctly identifies both P- and S-wave arrivals.

5.3 Full 14-Month Deployment (Unknown Arrival Times)

Whilst evaluating model performance on individual, manually scrutinized waveforms is useful for benchmarking and yielding estimates of model efficacy, the model's performance in a 'real-world' setting is ultimately of most importance to seismic analysts. Evaluating such performance is inherently more challenging, however, as the number of events in long sections of monitoring data and their respective phase arrival times are unknown, and other considerations, such as computational time and resources (e.g., memory requirements and availability of optimized hardware), affect model feasibility as a monitoring tool.

In this section, we present results of our best performing model in the prior section (U-GPD transfer learning model trained with full training dataset of 2498 samples of each class) and the original base GPD model when run over the full 14-month Nabro seismic deployment (Fig 8). As with the test dataset in Section 5.2, phase arrivals are detected at individual stations through a simple trigger algorithm, where an arrival is detected if the probability assigned to that class label (P or S) exceeds a given threshold (e.g., 0.4 for our U-GPD transfer learning model). The phase arrival time is determined as the waveform sample with the highest probability for that phase (Fig 7).

The U-GPD transfer learning model was applied to the data as a sliding window with 50 % overlap (i.e., applied at 'time shifts' of 200 samples) over 24-hour sections of data from each individual station. The model takes 5 seconds to process 24 hours of 3-component data at 100 Hz sample rate (or 3 seconds per day at 50 Hz sample rate) on a single graphics processing unit (GPU; NVIDIA GeForce RTX 2080 Ti), a rate many orders of magnitude faster than 'real-time' even when run on hundreds of stations. To avoid poor predictions due to window edge effects, only the middle 200 sample predictions out of 400 from each window are used to predict phase arrivals and are concatenated to produce one long continuous prediction trace without overlap or gaps and with the same sample rate as that of the input signal (i.e., 100 or 50 Hz). With all other processing steps

(e.g., software initialization, data read/write, signal windowing, running trigger algorithm, etc.), the U-GPD transfer learning model picks phase arrivals at all 7 available stations from the full 14-month deployment in less than 4 hours using a single GPU (greatly reduced when parallelized over multiple GPUs), indicating that it could easily be used within real-time monitoring constraints.

Conversely, as the GPD model produces only one class prediction per window (Fig 1A), we apply this model with much greater overlap (97.5 %; every 10 samples of data) and with varying threshold values (0.9, 0.95 and 0.99) for phase arrival detection triggering. This generates a prediction trace with a much coarser sample rate than the original input signal (i.e., from 100 or 50 Hz to 10 or 5 Hz, respectively) and takes 26 seconds per 24 hours' 3-component data at 100 Hz sample rate (or 15 seconds per day at 50 Hz sample rate) on the same NVIDIA GPU, approximately a five-fold increase in computational time with a tenth of the temporal detail. With all other processing steps, the GPD model took almost 50 hours to run over the full 14-month deployment using a single GPU, more than a ten-fold increase in computational time over the transfer learning model, due to more (pre-)processing required (e.g., more signal windows generated and subsequent processing). Assuming a linear increase in computational time, running the model as a sliding window over every sample of data would take ~ 260 seconds per 24 hours' 3-component data at 100 Hz sample rate and ~ 500 hours (nearly 3 weeks) for the full 14-month deployment and 7 stations. While this is still faster than real-time, these timescales for a single or limited number of station(s) could become limiting when applied at hundreds of stations, particularly without high performance computing resources.

5.3.1 Phase Association Method

Both models detect P- and S-wave phase arrivals but do not associate them to the same event. To assess the number of locatable events detected, we group P-wave phase arrival triggers into 4-second bins and keep only bins with arrivals detected at four or more stations. This bin size was chosen to encompass the maximum plausible travel time between any two stations. If multiple arrivals were detected at the same station within a 4-second bin, the detection threshold was increased for all arrivals in that particular bin to retain only the highest probability phase picks. If

any of these bins now had arrivals at less than four stations, as a result of removing lower probability phase picks, they were discarded as there would be too few stations to constrain event location. If there were still multiple arrivals present at any given station, only the arrivals with highest probability for each station were kept. Finally, if phase arrival bins intersected (a subset of one bin was contained in another), the bin with highest mean probability was kept. This association method is clearly quite crude, and only works for small, very local arrays, but allows a broad evaluation of model performance at detecting phase arrivals. Use of a more rigorous phase association method (e.g., Ross et al., 2019; Yeck et al., 2019) would obviously be better at eliminating false arrival picks or identifying multiple events within a 4 second window, which is a common feature of seismicity during volcanic unrest. However, this will mask underlying model performance; e.g., the inclusion of false arrival picks is likely to generate greater estimated location errors (Fig 10).

We associate S-wave arrivals to their corresponding P-wave arrivals by first locating events using NonLinLoc (e.g., Lomax et al., 2000), a widely used software package for probabilistic earthquake location, using the P-wave arrival bins outlined above (Fig 8A) and a simple 1D linear gradient velocity model from previous seismic studies at Nabro (Table S8; Goitom et al., 2015; Hamlyn et al., 2014). The difference between P-wave arrival and event origin times were used to predict which S-wave arrival detections should be associated with each P-wave arrival using a Vp/Vs ratio of 1.76 (Goitom et al., 2015) and S-wave travel time error of 0.25 (25%). S-wave arrival triggers that lay within this error bound for each detected P-wave arrival were associated to that event. S-wave arrivals at stations without a detected P-wave arrival were not included. All events were then located again in NonLinLoc using all included phase arrivals (Fig 8B).

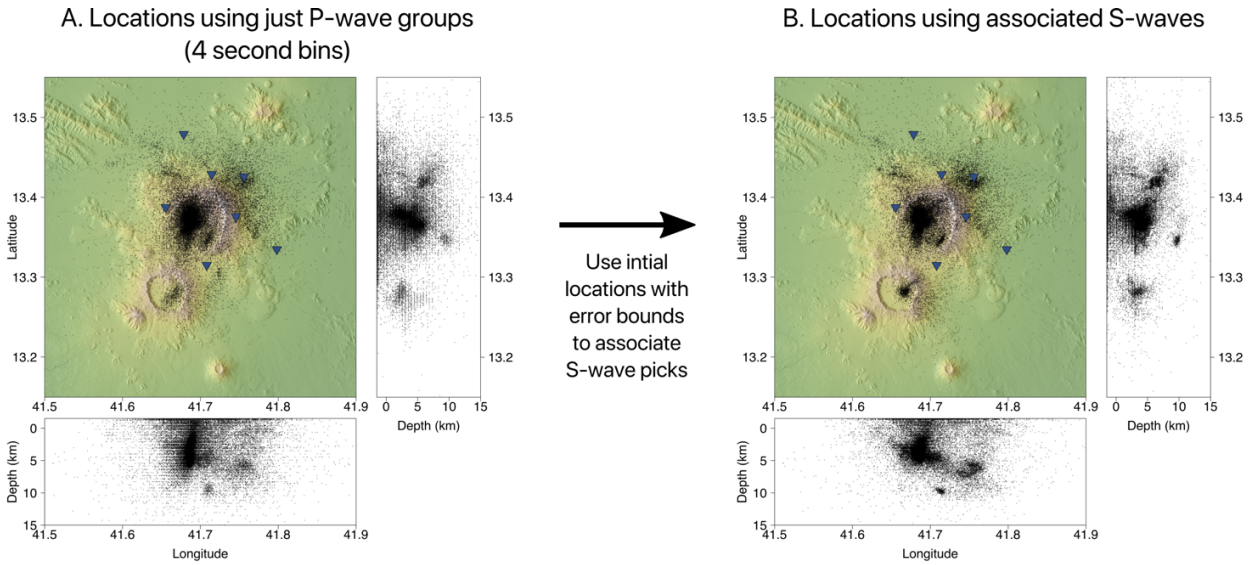

Figure 8. U-GPD transfer learning model event locations (total no. of events = 33,950) using automated phase association strategy. **A)** P-wave phase arrival triggers are grouped into 4 second bins and these groupings are used to obtain initial event hypocenters and origin times. **B)** S-wave phase arrival triggers are associated to P-waves in (**A**) using initial origin times, a Vp/Vs ratio of 1.76 and a travel-time error of 25 %. Events are then located again using all included P-wave and S-wave arrivals.

5.3.2 Detected Events and Location Errors

Figure 9 shows the cumulative number of events detected by the U-GPD transfer learning model (threshold value of 0.4; black solid line) and the original GPD model (threshold values of 0.9, 0.95 and 0.99; grey lines). The cumulative number of events from an existing manual catalogue for this deployment (Goitom, 2017; Hamlyn et al., 2014), some of which provided the transfer learning model training data, is also given for reference. Event locations for each model and the manual catalogue are provided in Supplementary Materials (Figs S3 – S6). When only P-wave arrivals are used (Fig 9A), the GPD model with detection threshold of 0.9 appears to detect the most events (total no. of events detected by GPD model = 41,007; total no. of events detected by transfer learning model = 33,950). A threshold of 0.95 also detects more events than the transfer learning model until shortly after the switch in instrument sample rates from 100 Hz to 50 Hz.

749 However, when we consider events with at least one associated S-wave arrival, the transfer
750 learning model detects more events overall (Fig 9B; no. of events detected by transfer learning
751 model = 31,387; no. of events detected by GPD model with 0.9 threshold = 26,808). This is
752 consistent with the results from our test dataset in Section 5.2, with the proportion of S-wave
753 arrivals accurately detected by the GPD model at these threshold values much lower than the
754 proportion of P-wave arrivals detected (Fig 5B – D). Furthermore, 6 % of noise waveforms and
755 16% of S-wave arrivals from our test data were mislabeled by the GPD model (0.9 threshold value)
756 as P-wave arrivals (Fig 5B), a higher rate of false detections or labels than the transfer learning
757 model (1 % of noise sections and 0.5% of S-waves, respectively; Fig 5G). This means that a higher
758 proportion of the P-wave groupings detected by this model with 0.9 threshold value are likely to
759 include mislabeled S-waves or false arrivals, which is reflected in subsequent event location errors
760 (Fig 10C – D).
761

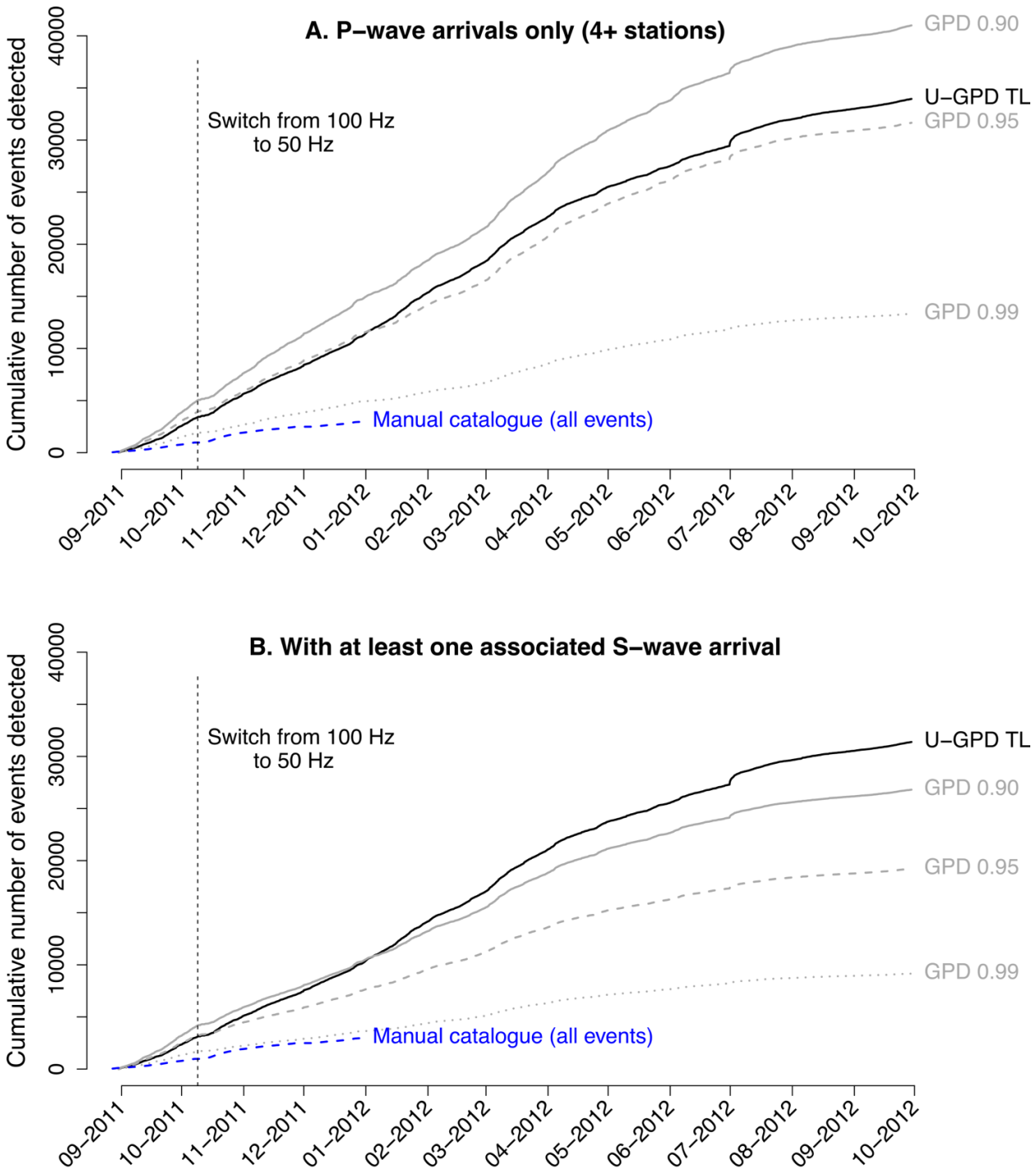

Figure 9. Cumulative number of events detected by GPD model (various thresholds, grey lines) and transfer learning model trained on full Nabro dataset (2498 samples of each class, 0.4 threshold, black line). Blue dashed line is existing manual catalogue (Goitom, 2017). All training / validation waveforms are from dates before switch in sample frequency (vertical dashed line).

768 **A)** Cumulative number of events detected using P-wave arrivals only (see main text for event
769 binning procedure). **B)** Cumulative number of events with at least one associated S-wave arrival.
770
771 To scrutinize these results further, we examine the number of stations with P- and S-wave
772 arrival detections per event (Fig 10A – B). In general, the events detected and picked by the U-
773 GPD transfer learning model include more stations and considerably more S-wave arrivals than
774 those picked by the GPD model, although the number detected by the GPD model may have been
775 reduced by using a coarser prediction trace (every 10 samples, a requirement to reduce model run
776 time to a reasonable timeframe). This increase in the number of stations and S-wave arrivals per
777 event will constrain event locations, as seen in the location errors derived from the models' phase
778 arrival picks (Fig 10C – D).
779
780 Location errors are estimated by NonLinLoc using multi-dimensional Gaussian estimators
781 and subsequent confidence intervals (e.g., Lomax et al., 2000). The horizontal errors (Fig 10C) for
782 the locations produced using the transfer learning model pick times are comparable to the existing
783 manually picked events. Furthermore, vertical (depth) errors are much improved over the manual
784 catalogue (Fig 10D), likely reflecting more consistency in S-wave arrival picking than that of a
785 manual analyst. The GPD model, by comparison, produces a more diffuse range of horizontal and
786 vertical errors, which is likely to be a combination of coarser prediction trace, poorer pick precision
787 (Fig 6A), lack of S-wave arrivals (Fig 10B) and false/mislabeled P-wave arrival detections (Fig
788 5B). This interpretation is further supported when we look at the number of event locations lying
789 within the array (i.e., event locations lying within the convex hull of station coordinates) for each
790 model: NonLinLoc locates more events within the array using the transfer learning picks (n =
791 23,859) than using the GPD model with 0.9 threshold value (n = 22,826). While we expect many
792 events to occur outside of the array (e.g., at neighboring faults or volcanic centres), this metric
793 shows that a much larger proportion of event locations detected by the GPD model lie away from
794 the volcanic edifice, which may reflect poorer pick precision, false/mislabeled arrivals or coarser
795 prediction trace, but may also reflect the event types (i.e., regional tectonic) that the original model
796 was trained on.
797

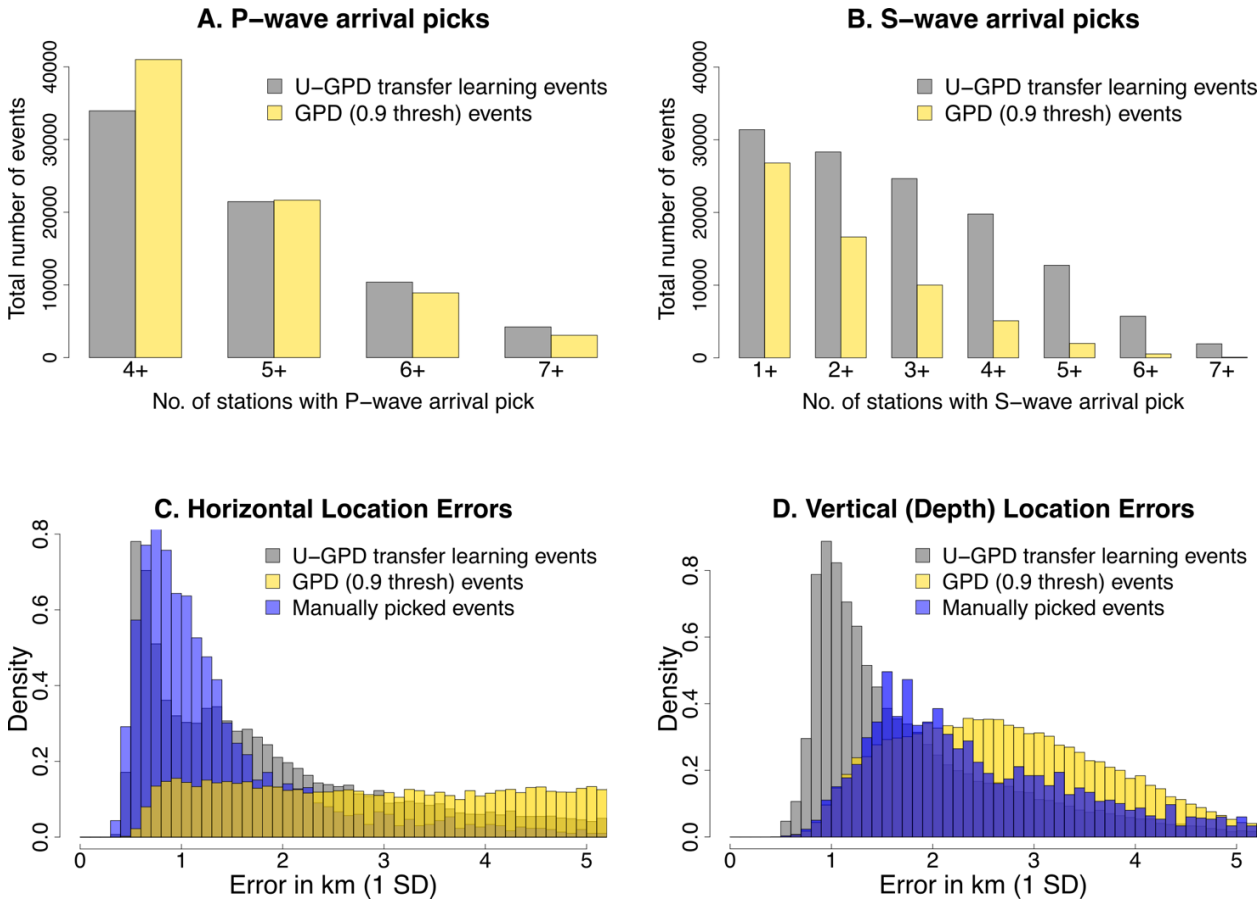

Figure 10. A) Number of P-wave arrival picks per event for transfer learning model (grey) and base GPD model (gold). **B)** Number of S-wave arrival picks per event. **C)** Histogram of Gaussian horizontal location errors (1 standard deviation) for events picked by transfer learning model (grey) and base GPD model (gold), and those in the existing manual catalogue (blue). **D)** Histogram of Gaussian vertical (depth) location errors (1 standard deviation).

6 Discussion

Transfer learning using existing seismological deep learning models can be a highly effective strategy to automate phase arrival picking in settings with little or no prior monitoring. We demonstrate that, with a limited number of hand-labelled waveforms (on the order of hundreds to low thousands) and a few minutes of training time, one can produce a consistent and effective

812 deep learning model for phase arrival detection that requires no other manual intervention or tuning
813 and can process years of data in a matter of hours.
814
815 For small training datasets, the use of pre-existing, generalized CNN filters greatly reduces
816 model overfitting (i.e., model parameters 'memorizing' the training data) when compared with
817 training a model from scratch (Fig 3) and yields a more stable relationship between maximizing
818 model accuracy and minimizing model error (Fig 4). Furthermore, when combined with a good
819 data augmentation strategy, transfer learning can also address the issue of processing data when
820 instrument sample rates differ from those used to train existing models. When applied to data from
821 Nabro volcano, augmenting our training set with decimated waveforms greatly improves model
822 performance on lower sample rate data (Fig S2). As such, hand-labelled training data from the first
823 35 days of the deployment (all 100 Hz sample rate) were sufficient to detect phase arrivals
824 throughout the duration of the deployment, even after instrument sample rates were switched to
825 50 Hz (Fig 9). Without this data augmentation step, model performance on lower sample rate data
826 declines dramatically (Fig S2). This shows that where sample rates are altered or new instruments
827 added during a seismic deployment, data augmentation can overcome the cost of collecting further
828 hand-labelled data and allow models to be adapted cheaply and quickly throughout the
829 deployment.
830
831 The introduction of new, task-specific data and the change in model task from one of
832 classification to one of segmentation also improves our U-GPD model pick time precision (Fig 6),
833 the number of stations per detected event (Fig 10A), the number of S-wave arrivals detected (Figs
834 5 and 10B) and computational efficiency over the original base GPD model, as well as potentially
835 reducing the number of false/mislabeled P-wave detections (Fig 5) and increasing the number of
836 identified events that relate directly to volcanic activity (evidenced by the increased number of
837 events located within the array). Without manual intervention or sophisticated phase association,
838 phase arrival picks from the U-GPD transfer learning model produce locations with smaller depth
839 errors than the base GPD model and even manually determined phase arrival times (Fig 10D). This
840 is likely a result of more consistent picking and labelling, particularly for S-wave arrivals, which
841 is difficult even for manual analysts to perform consistently, and suggests that very few of the
842 events detected are false.

Given the greatly improved computational time over the base GPD model, the small number of training events required and the use of a high-level, user-focused programming library (Keras), this approach is well within the reach of volcano observatories and research groups. Previous studies that analyze the pre-, syn- and post-eruptive periods at Nabro volcano have relied on manually-produced seismic catalogues comprising hundreds of events (e.g., Goitom et al., 2015; Hamlyn et al., 2014; the latter locating 658 events over 38 days, a rate of < 18 events per day). Our U-GPD transfer learning model yields a seismic catalogue that is order of magnitudes larger (33,950 events over 396 days, a rate of > 85 events per day; Figs 8 and 9), with smaller location errors (Fig 10), in a matter of hours. Furthermore, as the model processes 1D waveform data, as opposed to 2D spectrogram images in some other existing models (e.g., Dokht et al., 2019; Lara et al., 2020; Titos et al., 2020), it runs quickly on high resolution data without using a GPU optimized for deep learning frameworks (32 secs per 24 hours of 100 Hz data on an Intel Core i7 desktop CPU) and so could easily be deployed for real-time monitoring with limited computing resources or at much larger arrays. The methods and computational times in this paper have relied on standard, generic libraries (ObsPy, TensorFlow and Keras); the use of more optimized, compiled code or higher-performance / lower-level languages (e.g., Julia and C) could greatly improve computational times further.

Beyond phase arrival picking, the generalized waveform features extracted by existing, extensively trained models, such as the GPD model (Fig 1A), could serve as a useful feature extraction system for models designed for other waveform processing tasks. For example, information regarding frequency content and orientation of seismic energy extracted by the GPD model (Fig 1A inset) could reasonably provide useful features for a new model designed to automatically classify volcano seismic event types (e.g., Bueno et al., 2020; Hibert et al., 2017; Lara et al., 2020), particularly when available annotated datasets are small or unbalanced. However, with larger datasets, there is the potential for transfer learning to inhibit learning of new, useful features, particularly if the source and target tasks or data distributions differ considerably.

The number of seismological studies to date that employ transfer learning is relatively low (e.g., Bueno et al., 2020; Chai et al., 2020; El Zini et al., 2020; Huot et al., 2018; Titos et al., 2020).

This is undoubtedly, in part, due to the lack of extensively trained, well-documented, publicly available seismological models. However, the number is likely to grow as more extensive datasets and models are developed and released into the public domain. We credit the availability of the GPD model in the public domain and use of a popular, user-focused machine learning framework (Keras) as the foundation of the work presented in this paper. Such availability facilitates adaptation and experimentation; development of other publicly available models and extensive datasets would aid progress in the field of seismological machine learning.

Whilst the application of transfer learning can overcome the perception that deep learning models require a 'large upfront cost' in terms of data and computational resources, the development and benchmarking of large-scale, extensive models and datasets are still imperative to push the field of seismological machine learning forwards and extend applications to all aspects of seismic processing and inference. However, it is hoped that applications such as the one presented in this paper will motivate the initial investment in the development of such models so that the cost of producing effective task-specific models (e.g., through transfer learning) is progressively reduced.

Acknowledgments

The seismic data were collected with funding from the Natural Environment Research Council (NERC) project NE/J012297/1 ("Mechanisms and implications of the 2011 eruption of Nabro volcano, Eritrea"). The UK seismic instruments and data management facilities were provided under loan number 976 by SEIS-UK at the University of Leicester. The facilities of SEIS-UK are supported by NERC under Agreement R8/H10/64. Author SL was supported by a GW4+ Doctoral Training Partnership studentship from the Natural Environment Research Council (NERC) [NE/L002434/1]. Author BG was funded by the Engineering and Physical Sciences Research Council (EPSRC) and the School of Earth Sciences at the University of Bristol. Author MJW was funded by UKRI GCRF EP/P028233/1 ("PREPARE") and NERC NE/R017956/1 ("EQUIPT4RISK"). Author JMK was funded by NERC grant NE/R018006/1. Author KVC

was supported by the AXA Research Fund. We gratefully acknowledge support from the sponsors of the Bristol University Microseismicity ProjectS (BUMPS) and the NERC Centre for the Observation and Modelling of Earthquakes, volcanoes and Tectonics (COMET). We also gratefully acknowledge the cooperation we received from the Eritrea Institute of Technology, Eritrean government, Southern and Northern Red Sea Administrations, local sub-zones and village administrations. We thank the Department of Mines, Ministry of Energy and Mines for their continued support throughout the project. Special thanks go to Zerai Berhe, Mebrahtu Fisseha, Michael Eyob, Ahmed Mohammed, Kibrom Nerayo, Asresehey Ogbatsien, Andemichael Solomon and Isaac Tuum. We thank Alem Kibreab and Prof. Ghebrebrhan Ogubazghi for their vital help in facilitating the fieldwork.

Data Availability Statement

All seismic data from the Nabro Urgency Array (Hammond et al., 2011; https://doi.org/10.7914/SN/4H_2011) are publicly available through IRIS Data Services (http://service.iris.edu/fdsnws/dataselect/1/). IRIS Data Services are funded through the Seismological Facilities for the Advancement of Geoscience (SAGE) Award of the National Science Foundation under Cooperative Support Agreement EAR-1851048. See Hammond et al. (2011) for further details on waveform data access and availability. Model training, validation and test sets / metadata are archived and available through Zenodo (Lapins et al., 2021; https://doi.org/10.5281/zenodo.4498549). Full code to reproduce our U-GPD transfer learning model, perform model training, run the U-GPD model over continuous sections of data and use model picks to locate events in NonLinLoc (Lomax et al., 2000) are available at https://github.com/sachalapins/U-GPD, with the release (v1.0.0) associated with this paper also archived and available through Zenodo (Lapins, 2021; https://doi.org/10.5281/zenodo.4558121).

References

Abadi, M., Agarwal, A., Barham, P., Brevdo, E., Chen, Z., Citro, C., … Zheng, X. (2015). TensorFlow: Large-Scale Machine Learning on Heterogeneous Distributed Systems (software available from https://www.tensorflow.org).

Barbedo, J. G. A. (2018). Impact of dataset size and variety on the effectiveness of deep learning and transfer learning for plant disease classification. Computers and Electronics in Agriculture, 153, 46–53. https://doi.org/10.1016/j.compag.2018.08.013

Bergstra, J, Bengio, Y. (2012). Random Search for Hyper-Parameter Optimization. *Journal of Machine Learning Research, 13*(10), 281-305.

Beyreuther, M., Barsch, R., Krischer, L., Megies, T., Behr, Y., & Wassermann, J. (2010). ObsPy: A python toolbox for seismology. *Seismological Research Letters*, *81*(3), 530–533. https://doi.org/10.1785/gssrl.81.3.530

Bojanowski, A. (2011). Volcano mix-up. *Nature Geoscience*, *4*(8), 495. https://doi.org/10.1038/ngeo1222

Bueno, A., Benitez, C., De Angelis, S., Diaz Moreno, A., & Ibanez, J. M. (2020). Volcano-Seismic Transfer Learning and Uncertainty Quantification with Bayesian Neural Networks. *IEEE Transactions on Geoscience and Remote Sensing*, *58*(2), 892–902. https://doi.org/10.1109/TGRS.2019.2941494

Chai, C., Maceira, M., Santos-Villalobos, H. J., Venkatakrishnan, S. V., Schoenball, M., Zhu, W., … Thurber, C. (2020). Using a Deep Neural Network and Transfer Learning to Bridge Scales for Seismic Phase Picking. *Geophysical Research Letters*, *47*(16). https://doi.org/10.1029/2020GL088651

Chollet, F., & and others. (2015). Keras (software available from https://keras.io).

D'souza, R. N., Huang, P.-Y., & Yeh, F.-C. (2020). Structural Analysis and Optimization of Convolutional Neural Networks with a Small Sample Size. *Scientific Reports*, *10*(834). https://doi.org/10.1038/s41598-020-57866-2

Daumé, H. (2007). Frustratingly easy domain adaptation. In *45th Annual Meeting of the Association for Computational Linguistics (ACL)* (pp. 256–263). https://arxiv.org/abs/0907.1815

Dokht, R. M. H., Kao, H., Visser, R., & Smith, B. (2019). Seismic Event and Phase Detection Using Time–Frequency Representation and Convolutional Neural Networks. *Seismological Research Letters*, *90*(2A), 481–490. https://doi.org/10.1785/0220180308

Donovan, A., Blundy, J., Oppenheimer, C., & Buisman, I. (2018). The 2011 eruption of Nabro volcano, Eritrea: perspectives on magmatic processes from melt inclusions. *Contributions to Mineralogy and Petrology*, *173*(1), 1–23. https://doi.org/10.1007/s00410-017-1425-2

Dramsch, J. S., & Lüthje, M. (2018). Deep-learning seismic facies on state-of-the-art CNN architectures. In *SEG Technical Program Expanded Abstracts* (pp. 2036–2040). Anaheim, CA, USA.

Efremova, Di. B., Sankupellay, M., & Konovalov, D. A. (2019). Data-Efficient Classification of Birdcall through Convolutional Neural Networks Transfer Learning. In *2019 Digital Image Computing: Techniques and Applications (DICTA)* (pp. 1–8). Perth, Australia. https://doi.org/10.1109/DICTA47822.2019.8946016

El Zini, J., Rizk, Y., & Awad, M. (2020). A Deep Transfer Learning Framework for Seismic Data Analysis: A Case Study on Bright Spot Detection. *IEEE Transactions on Geoscience and Remote Sensing*, *58*(5), 3202–3212. https://doi.org/10.1109/TGRS.2019.2950888

Feurer, M., Klein, A., Eggensperger, K., Springenberg, J., Blum, M., & Hutter, F. (2015). Efficient and Robust Automated Machine Learning. In *Advances in Neural Information Processing Systems 28 (NIPS 2015),* 2962-2970.

Fromm, M., Kablick III, G., Nedoluha, G., Carboni, E., Grainger, R., Campbell, J., & Lewis, J. (2014). Correcting

the record of volcanic stratospheric aerosol impact: Nabro and Sarychev Peak. *Journal of Geophysical Research: Atmospheres*, *119*, 10343–10364. https://doi.org/10.1002/2014JD021507

Ganin, Y., Ustinova, E., Ajakan, H., Germain, P., Larochelle, H., Laviolette, F., … Lempitsky, V. (2016). Domain-Adversarial Training of Neural Networks. *Journal of Machine Learning Research*, *17*(59), 1–35. https://arxiv.org/abs/1505.07818

Gibbons, S. J., & Ringdal, F. (2006). The detection of low magnitude seismic events using array-based waveform correlation. *Geophysical Journal International*, *165*(1), 149–166. https://doi.org/10.1111/j.1365-246X.2006.02865.x

Global Volcanism Program. (2013). Volcanoes of the World, v.4.9.3 (01 Feb 2021). Venzke, E (ed.). Smithsonian Institution. Downloaded 10 Feb 2021. https://doi.org/10.5479/si.GVP.VOTW4-2013

Glorot, X., Bordes, A., & Bengio, Y. (2011). Domain adaptation for large-scale sentiment classification: A deep learning approach. In *Proceedings of the 28th International Conference on Machine Learning, ICML 2011* (pp. 513–520). Bellevue, WA, USA.

Goitom, B. (2017). The Nabro volcano, tectontic framework and seismic hazard assessment of Eritrea [doctoral thesis]. University of Bristol.

Goitom, B., Oppenheimer, C., Hammond, J. O. S., Grandin, R., Barnie, T., Donovan, A., … Berhe, S. (2015). First recorded eruption of Nabro volcano , Eritrea , 2011. *Bulletin of Volcanology*, *77*(85). https://doi.org/10.1007/s00445-015-0966-3

Hamlyn, J. E., Keir, D., Wright, T. J., Neuberg, J. W., Goitom, B., Hammond, J. O. S., … Grandin, R. (2014). Seismicity and subsidence following the 2011 Nabro eruption, Eritrea: Insights into the plumbing system of an off-rift volcano. *Journal of Geophysical Research: Solid Earth*, *119*, 8267–8282. https://doi.org/10.1002/2014JB011395

Hammond, J., Goitom, B., Kendall, J. M., Ogubazghi, G. (2011). Nabro Urgency Array [Data set]. International Federation of Digital Seismograph Networks. https://doi.org/10.7914/SN/4H_2011

Hansen, S. M., & Schmandt, B. (2015). Automated detection and location of microseismicity at Mount St. Helens with a large-N geophone array. *Geophysical Research Letters*, *42*(18), 7390–7397. https://doi.org/10.1002/2015GL064848

He, T., Zhang, Z., Zhang, H., Zhang, Z., Xie, J., & Li, M. (2019). Bag of Tricks for Image Classification with Convolutional Neural Networks. In *2019 IEEE/CVF Conference on Computer Vision and Pattern Recognition (CVPR)* (pp. 558–567). Long Beach, CA, USA. https://doi.org/10.1109/CVPR.2019.00065

Hibert, C., Provost, F., Malet, J. P., Maggi, A., Stumpf, A., & Ferrazzini, V. (2017). Automatic identification of rockfalls and volcano-tectonic earthquakes at the Piton de la Fournaise volcano using a Random Forest algorithm. *Journal of Volcanology and Geothermal Research*, *340*, 130–142. https://doi.org/10.1016/j.jvolgeores.2017.04.015

Huot, F., Biondi, B., & Beroza, G. C. (2018). Jump-starting neural network training for seismic problems. In *SEG Technical Program Expanded Abstracts* (pp. 2191–2195).

Ioffe, S., & Szegedy, C. (2015). Batch normalization: Accelerating deep network training by reducing internal

covariate shift. In *32nd International Conference on Machine Learning (ICML)* (pp. 448–456). Lille, France. https://arxiv.org/abs/1502.03167

Kingma, D. P., & Ba, J. (2014). Adam: A Method for Stochastic Optimization. In *3rd International Conference on Learning Representations (ICLR)* (pp. 1–15). http://arxiv.org/abs/1412.6980

Kirkpatrick, J., Pascanu, R., Rabinowitz, N., Veness, J., Desjardins, G., Rusu, A. A., … Hadsell, R. (2017). Overcoming catastrophic forgetting in neural networks. *Proceedings of the National Academy of Sciences*, *114*(13), 3521–3526. https://doi.org/10.1073/pnas.1611835114

Klein, A., Falkner, S., Bartels, S., Henning, P., & Hutter, F. (2017). Fast Bayesian Optimization of Machine Learning Hyperparameters on Large Datasets. *Proceedings of the 20th International Conference on Artificial Intelligence and Statistics, PMLR 54,* 528-536. https://arxiv.org/abs/1605.07079

Krischer, L., Megies, T., Barsch, R., Beyreuther, M., Lecocq, T., Caudron, C., & Wassermann, J. (2015). ObsPy: A bridge for seismology into the scientific Python ecosystem. *Computational Science and Discovery*, *8*, 014003. https://doi.org/10.1088/1749-4699/8/1/014003

Lahr, J. C., Chouet, B. A., Stephens, C. D., Power, J. A., & Page, R. A. (1994). Earthquake classification, location, and error analysis in a volcanic environment: implications for the magmatic system of the 1989–1990 eruptions at redoubt volcano, Alaska. *Journal of Volcanology and Geothermal Research*, *62*(1–4), 137–151. https://doi.org/10.1016/0377-0273(94)90031-0

Lapins, S. (2021). Python notebooks to accompany paper 'A Little Data goes a Long Way: Automating Seismic Phase Arrival Picking at Nabro Volcano with Transfer Learning' (Version v1.0.0) [Archived GitHub repository]. Zenodo. https://doi.org/10.5281/zenodo.4558121

Lapins, S., Goitom, B., Kendall, J.-M., Werner, M. J., Cashman, K. V. & Hammond, J. O. S. (2021). Training, Validation and Test Sets for paper 'A Little Data goes a Long Way: Automating Seismic Phase Arrival Picking at Nabro Volcano with Transfer Learning' [Dataset]. Zenodo. https://doi.org/10.5281/zenodo.4498549

Lapins, S., Roman, D. C., Rougier, J., De Angelis, S., Cashman, K. V, & Kendall, J.-M. (2020). An examination of the continuous wavelet transform for volcano-seismic spectral analysis. *Journal of Volcanology and Geothermal Research*, *389*, 106728. https://doi.org/10.1016/j.jvolgeores.2019.106728

Lara, F., Lara-Cueva, R., Larco, J. C., Carrera, E. V, & León, R. (2020). A deep learning approach for automatic recognition of seismo-volcanic events at the Cotopaxi volcano. *Journal of Volcanology and Geothermal Research*, (xxxx), 107142. https://doi.org/10.1016/j.jvolgeores.2020.107142

Lengliné, O., Duputel, Z., & Ferrazzini, V. (2016). Uncovering the hidden signature of a magmatic recharge at Piton de la Fournaise volcano using small earthquakes. *Geophysical Research Letters*, *43*(9), 4255–4262. https://doi.org/10.1002/2016GL068383

Li, H., Xu, Z., Taylor, G., Studer, C., & Goldstein, T. (2017). Visualizing the Loss Landscape of Neural Nets. *Advances in Neural Information Processing Systems (NIPS)*, 6389–6399. https://arxiv.org/abs/1712.09913

Li, W., Duan, L., Xu, D., & Tsang, I. W. (2014). Learning with augmented features for supervised and semi-supervised heterogeneous domain adaptation. *IEEE Transactions on Pattern Analysis and Machine Intelligence*, *36*(6), 1134–1148. https://doi.org/10.1109/TPAMI.2013.167

1047 Lin, T.-Y., Goyal, P., Girshick, R., He, K., & Dollar, P. (2017). Focal Loss for Dense Object Detection. In *2017*
1048 *IEEE International Conference on Computer Vision (ICCV)* (pp. 2999–3007). Venice, Italy: IEEE.
1049 https://doi.org/10.1109/ICCV.2017.324
1050 Lomax, A., Virieux, J., Volant, P., & Berge, C. (2000). Probabilistic earthquake location in 3D and layered models:
1051 Introduction of a Metropolis-Gibbs method and comparison with linear locations. In C. H. Thurber & N.
1052 Rabinowitz (Eds.), *Advances in Seismic Event Location* (pp. 101–134). Asterdam: Kluwer.
1053 Maclaurin, D., Duvenaud, D., & Adams, R. (2015). Gradient-based Hyperparameter Optimization through
1054 Reversible Learning. *Proceedings of the 32nd International Conference on Machine Learning, PLMR, 37,*
1055 2113-2122. https://arxiv.org/abs/1502.03492
1056 Maqsood, M., Nazir, F., Khan, U., Aadil, F., Jamal, H., Mehmood, I., & Song, O. (2019). Transfer Learning
1057 Assisted Classification and Detection of Alzheimer's Disease Stages Using 3D MRI Scans. *Sensors*, *19*(11),
1058 2645. https://doi.org/10.3390/s19112645
1059 McNutt, S. R., & Roman, D. C. (2015). Volcanic Seismicity. In *The Encyclopedia of Volcanoes* (2nd Edition, pp.
1060 1011–1034). Elsevier. https://doi.org/10.1016/B978-0-12-385938-9.00059-6
1061 Megies, T., Beyreuther, M., Barsch, R., Krischer, L., & Wassermann, J. (2011). ObsPy - what can it do for data
1062 centers and observatories? *Annals of Geophysics*, *54*(1), 47–58. https://doi.org/10.4401/ag-4838
1063 Mousavi, S. M., Ellsworth, W. L., Zhu, W., Chuang, L. Y. & Beroza, G. C. (2020). Earthquake transformer – an
1064 attentive deep-learning model for simultaneous earthquake detection and phase picking. *Nature*
1065 *Communications*, *11*, 3952. https://doi.org/10.1038/s41467-020-17591-w
1066 Mousavi, S. M., Zhu, W., Sheng, Y., & Beroza, G. C. (2019). CRED: A Deep Residual Network of Convolutional
1067 and Recurrent Units for Earthquake Signal Detection. *Scientific Reports*, *9*, 10267.
1068 https://doi.org/10.1038/s41598-019-45748-1
1069 Nair, V., & Hinton, G. E. (2010). Rectified Linear Units Improve Restricted Boltzmann Machines. In *Proceedings*
1070 *of the 27th International Conference on Machine Learning* (pp. 807–814). Haifa, Israel.
1071 https://doi.org/10.5555/3104322.3104425
1072 Pan, S. J., & Yang, Q. (2010). A survey on transfer learning. *IEEE Transactions on Knowledge and Data*
1073 *Engineering*, *22*(10), 1345–1359. https://doi.org/10.1109/TKDE.2009.191
1074 Razavian, A. S., Azizpour, H., Sullivan, J., & Carlsson, S. (2014). CNN features off-the-shelf: An astounding
1075 baseline for recognition. In *2014 IEEE Computer Society Conference on Computer Vision and Pattern*
1076 *Recognition Workshops* (pp. 512–519). Columbus, OH, USA: IEEE.
1077 https://doi.org/10.1109/CVPRW.2014.131
1078 Ronneberger, O., Fischer, P., & Brox, T. (2015). U-Net: Convolutional Networks for Biomedical Image
1079 Segmentation. In N. Navab, J. Hornegger, W. M. Wells, & A. F. Frangi (Eds.), *Medical Image Computing and*
1080 *Computer-Assisted Intervention (MICCAI) 2015, Part III, Lecture Notes in Computer Science* (Vol. 9351, pp.
1081 234–241). Springer International Publishing. https://doi.org/10.1007/978-3-319-24574-4_28
1082 Ross, Z. E., Meier, M., & Hauksson, E (2018a). P Wave Arrival Picking and First-Motion Polarity Determination
1083 With Deep Learning. *Journal of Geophysical Research: Solid Earth*, *123*(6), 5120-5129.

https://doi.org/10.1029/2017JB015251

Ross, Z. E., Meier, M., Hauksson, E., & Heaton, T. H. (2018b). Generalized Seismic Phase Detection with Deep Learning. *Bulletin of the Seismological Society of America*, *108*(5A), 2894–2901. https://doi.org/10.1785/0120180080

Ross, Z. E., Yue, Y., Meier, M., Hauksson, E., & Heaton, T. H. (2019). PhaseLink: A Deep Learning Approach to Seismic Phase Association. *Journal of Geophysical Research: Solid Earth, 124*(1), 856-869. https://doi.org/10.1029/2018JB016674

Shelly, D. R., Beroza, G. C., & Ide, S. (2007). Non-volcanic tremor and low-frequency earthquake swarms. *Nature*, *446*(7133), 305–307. https://doi.org/10.1038/nature05666

Shorten, C., & Khoshgoftaar, T. M. (2019). A survey on Image Data Augmentation for Deep Learning. *Journal of Big Data*, *6*(1). https://doi.org/10.1186/s40537-019-0197-0

Snoek, J., Rippel, O., Swersky, K., Kiros, R., Satish, N., Sundaram, N., Patwary, M. A., Prabhat, & Adams, R. P. (2015). Scalable Bayesian Optimization Using Deep Neural Networks. *Proceedings of the 32nd International Conference on Machine Learning, PMLR, 37*, 2171-2180. https://arxiv.org/abs/1502.05700

Sun, B., Feng, J., & Saenko, K. (2016). Return of frustratingly easy domain adaptation. In *30th AAAI Conference on Artificial Intelligence (AAAI)* (pp. 2058–2065). https://arxiv.org/abs/1511.05547

Sun, C., Shrivastava, A., Singh, S., & Gupta, A. (2017). Revisiting Unreasonable Effectiveness of Data in Deep Learning Era. In *2017 IEEE International Conference on Computer Vision (ICCV)* (pp. 843–852). Venice, 2017. https://doi.org/10.1109/ICCV.2017.97

Tan, Y. J., Waldhauser, F., Ellsworth, W. L., Zhang, M., Zhu, W., Michele, M., Chiaraluce, L., Beroza, G. C. & Segou, M. (2021). Machine-Learning-Based High-Resolution Earthquake Catalog Reveals How Complex Fault Structures Were Activated during the 2016 – 2017 Central Italy Sequence. *The Seismic Record*, *1*(1). https://doi.org/10.1785/0320210001

Theys, N., Campion, R., Clarisse, L., Brenot, H., van Gent, J., Dils, B., … Ferrucci, F. (2013). Volcanic SO2 fluxes derived from satellite data: a survey using OMI, GOME-2, IASI and MODIS. *Atmospheric Chemistry and Physics*, *13*, 5945–5968. https://doi.org/10.5194/acp-13-5945-2013

Titos, M., Bueno, A., García, L., Benítez, C., & Segura, J. C. (2020). Classification of Isolated Volcano-Seismic Events Based on Inductive Transfer Learning. *IEEE Geoscience and Remote Sensing Letters*, *17*(5), 869–873. https://doi.org/10.1109/LGRS.2019.2931063

Tompson, J., Goroshin, R., Jain, A., LeCun, Y., & Bregler, C. (2015). Efficient Object Localization Using Convolutional Networks. In *2015 IEEE Conference on Computer Vision and Pattern Recognition (CVPR)* (pp. 648–656). Boston, MA, USA: IEEE. https://doi.org/10.1109/CVPR.2015.7298664

Tran, K. T., Griffin, L. D., Chetty, K., & Vishwakarma, S. (2020). Transfer learning from audio deep learning models for micro-Doppler activity recognition. In *2020 IEEE International Radar Conference, (RADAR)* (pp. 584–589). Washington, DC, USA. https://doi.org/10.1109/RADAR42522.2020.9114643

Tzeng, E., Hoffman, J., Darrell, T., & Saenko, K. (2015). Simultaneous Deep Transfer Across Domains and Tasks. In *2015 IEEE International Conference on Computer Vision (ICCV)* (pp. 4068–4076). Santiago, Chile: IEEE.

https://doi.org/10.1109/ICCV.2015.463

van den Ende, M. P. A., & Ampuero, J. P. (2020). Automated Seismic Source Characterization Using Deep Graph Neural Networks. *Geophysical Research Letters*, *47*(17), 1–11. https://doi.org/10.1029/2020GL088690

van den Oord, A., Dieleman, S., Zen, H., Simonyan, K., Vinyals, O., Graves, A., … Kavukcuoglu, K. (2016). WaveNet: A Generative Model for Raw Audio. https://arxiv.org/abs/1609.03499

Withers, M., Aster, R., Young, C., Beiriger, J., Harris, M., Moore, S., & Trujillo, J. (1998). A comparison of select trigger algorithms for automated global seismic phase and event detection. *Bulletin of the Seismological Society of America*, *88*(1), 95–106.

Woollam, J., Rietbrock, A., Bueno, A., & De Angelis, S. (2019). Convolutional Neural Network for Seismic Phase Classification, Performance Demonstration over a Local Seismic Network. *Seismological Research Letters*, 1–12. https://doi.org/10.1785/0220180312

Yeck, W. L., Patton, J. M., Johnson C. E., Kragness, D., Benz, H. M., Earle, P. S., Guy, M. R., & Ambruz, N. B. (2019). GLASS3: A Standalone Multiscale Seismic Detection Associator. *Bulletin of the Seismological Society of America, 109*(4), 1469-1478. https://doi.org/10.1785/0120180308

Yosinski, J., Clune, J., Bengio, Y., & Lipson, H. (2014). How transferable are features in deep neural networks? *Advances in Neural Information Processing Systems*, *27*. https://arxiv.org/abs/1411.1792

Yu, F., & Koltun, V. (2016). Multi-scale context aggregation by dilated convolutions. In *4th International Conference on Learning Representations (ICLR)*. https://arxiv.org/abs/1511.07122

Zamir, A. R., Sax, A., Shen, W., Guibas, L., Malik, J., & Savarese, S. (2018). Taskonomy: Disentangling Task Transfer Learning. In *2018 IEEE/CVF Conference on Computer Vision and Pattern Recognition* (pp. 3712–3722). Salt Lake City, UT, USA: IEEE. https://doi.org/10.1109/CVPR.2018.00391

Zech, J. R., Badgeley, M. A., Liu, M., Costa, A. B., Titano, J. J., & Oermann, E. K. (2018). Variable generalization performance of a deep learning model to detect pneumonia in chest radiographs: A cross-sectional study. *PLOS Medicine*, *15*(11), 1–17. https://doi.org/10.1371/journal.pmed.1002683

Zhu, W., & Beroza, G. C. (2019). PhaseNet: a deep-neural-network-based seismic arrival-time picking method. *Geophysical Journal International*, *216*(1), 261–273. https://doi.org/10.1093/gji/ggy423

Zhuang, F., Cheng, X., Luo, P., Pan, S. J., & He, Q. (2015). Supervised representation learning: Transfer learning with deep autoencoders. In *IJCAI International Joint Conference on Artificial Intelligence* (pp. 4119–4125). Buenos Aires, Argentina.

Zhuang, F., Qi, Z., Duan, K., Xi, D., Zhu, Y., Zhu, H., … He, Q. (2020). A Comprehensive Survey on Transfer Learning. *Proceedings of the IEEE*, 1–34. https://doi.org/10.1109/JPROC.2020.3004555

Journal of Geophysical Research: Solid Earth

Supporting Information for

A Little Data goes a Long Way: Automating Seismic Phase Arrival Picking at Nabro Volcano with Transfer Learning

Sacha Lapins[1], Berhe Goitom[1], J-Michael Kendall[2], Maximilian J. Werner[1], Katharine V. Cashman[1] and James O. S. Hammond[3]

[1]School of Earth Sciences, University of Bristol, UK; [2]Department of Earth Sciences, University of Oxford, UK; [3]Department of Earth and Planetary Sciences, Birkbeck, University of London, UK.

Corresponding author: Sacha Lapins (sacha.lapins@bristol.ac.uk)

Contents of this file

Introduction

In this supporting information document, we provide full details of our U-GPD model architecture (Fig S1), cross-entropy loss function used for model training (Text S7), velocity model used to associate detected phase arrivals and locate events (Table S8), and comparisons of U-GPD model performance on test data using varying levels of data augmentation (Fig S2). We also provide plotted locations using the U-GPD model, base GPD model (with two threshold values) and existing manual catalogue (Figs S3-S6).

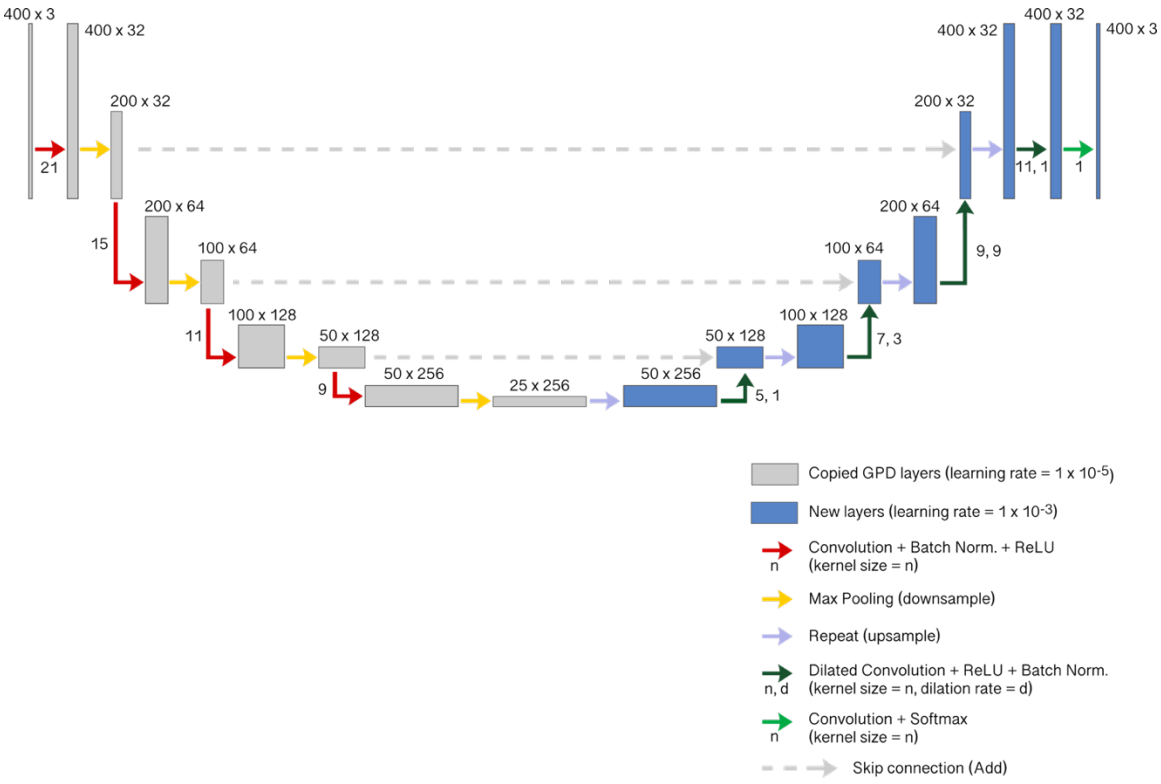

Figure S1. U-GPD model architecture.

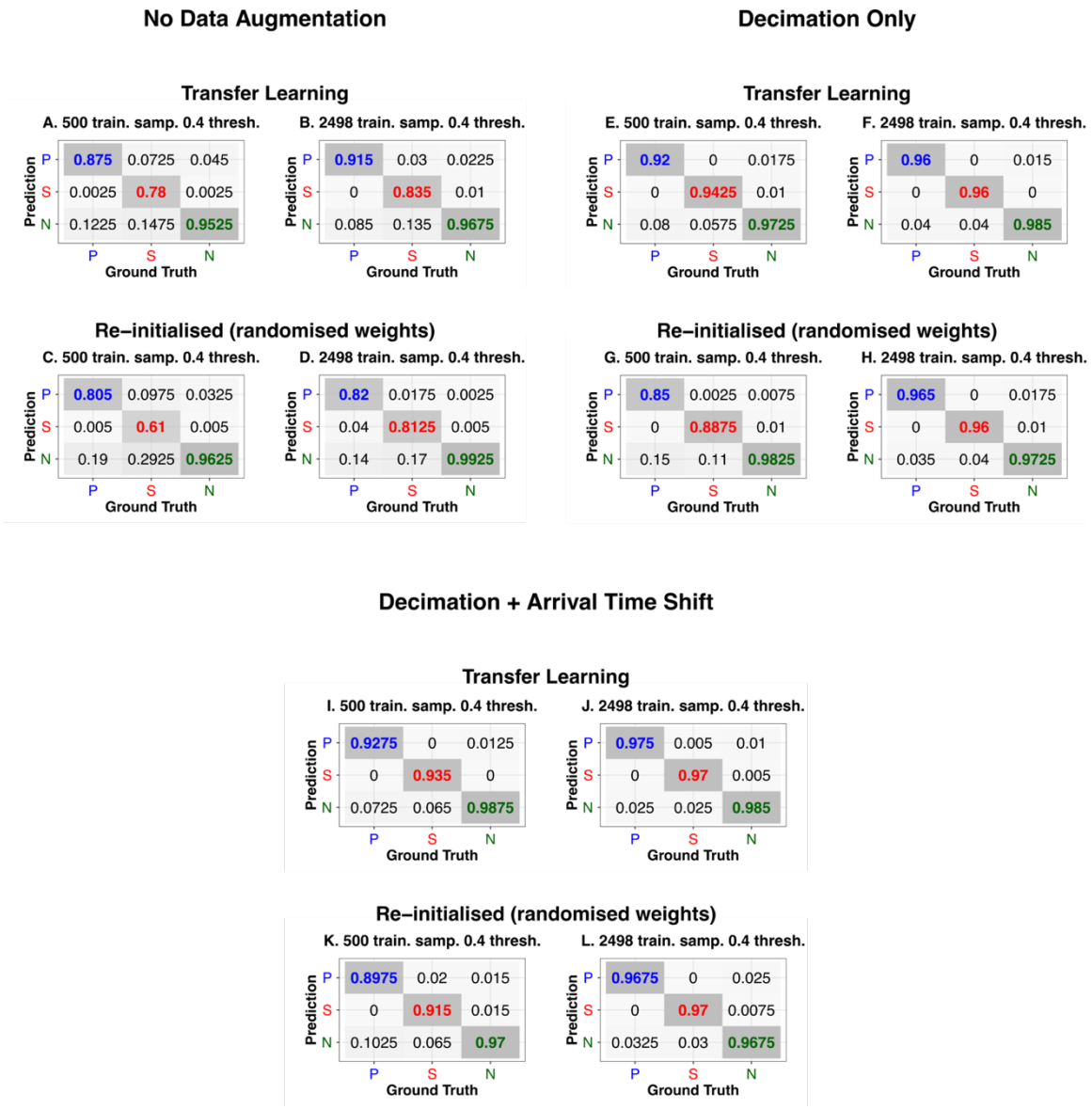

Figure S2. Results of U-GPD model, trained with different levels of data augmentation, applied to our test dataset.

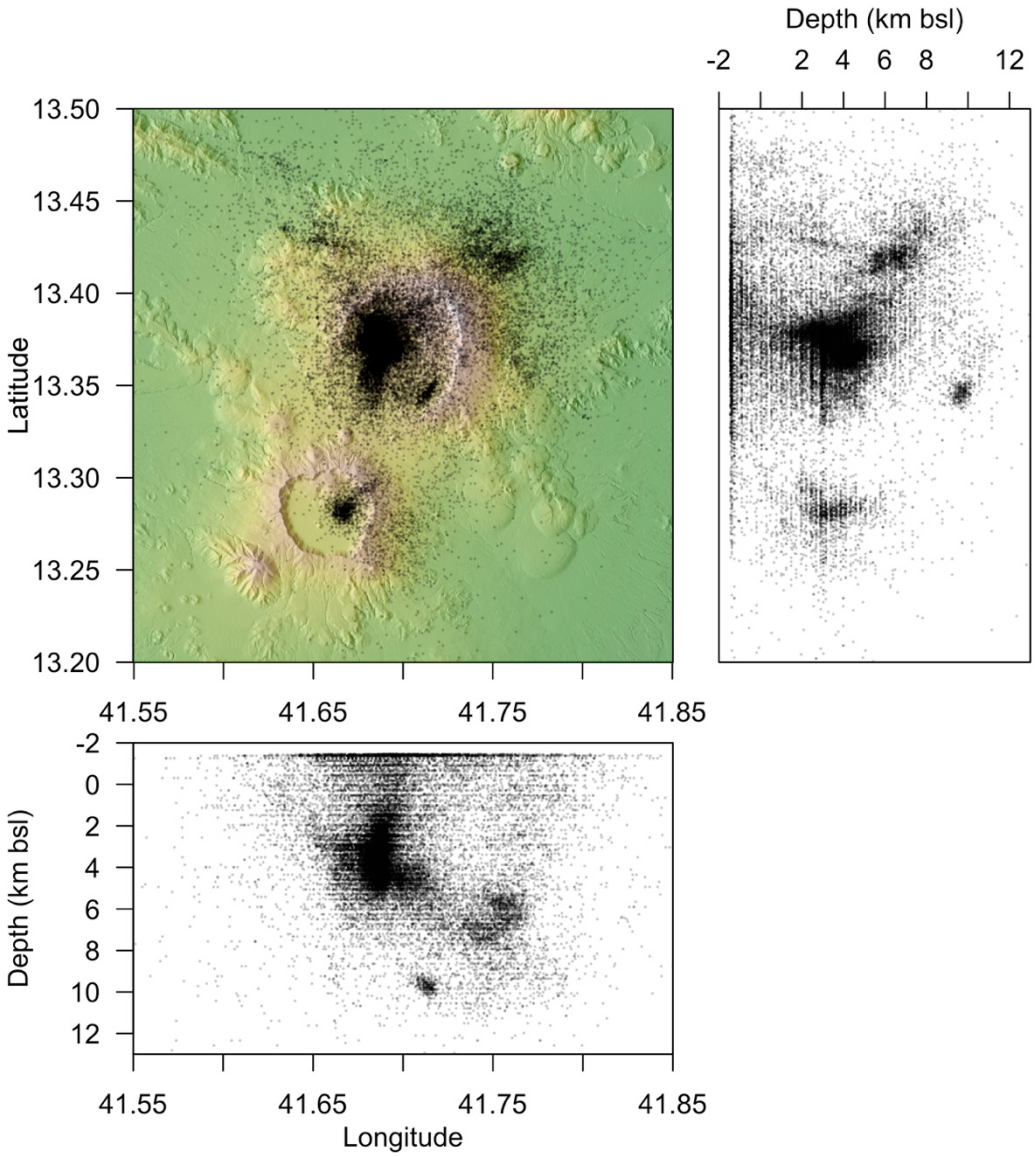

Figure S3. Event locations using P- and S-wave phase arrivals detected by U-GPD model with 0.4 threshold (no. of events = 33,950).

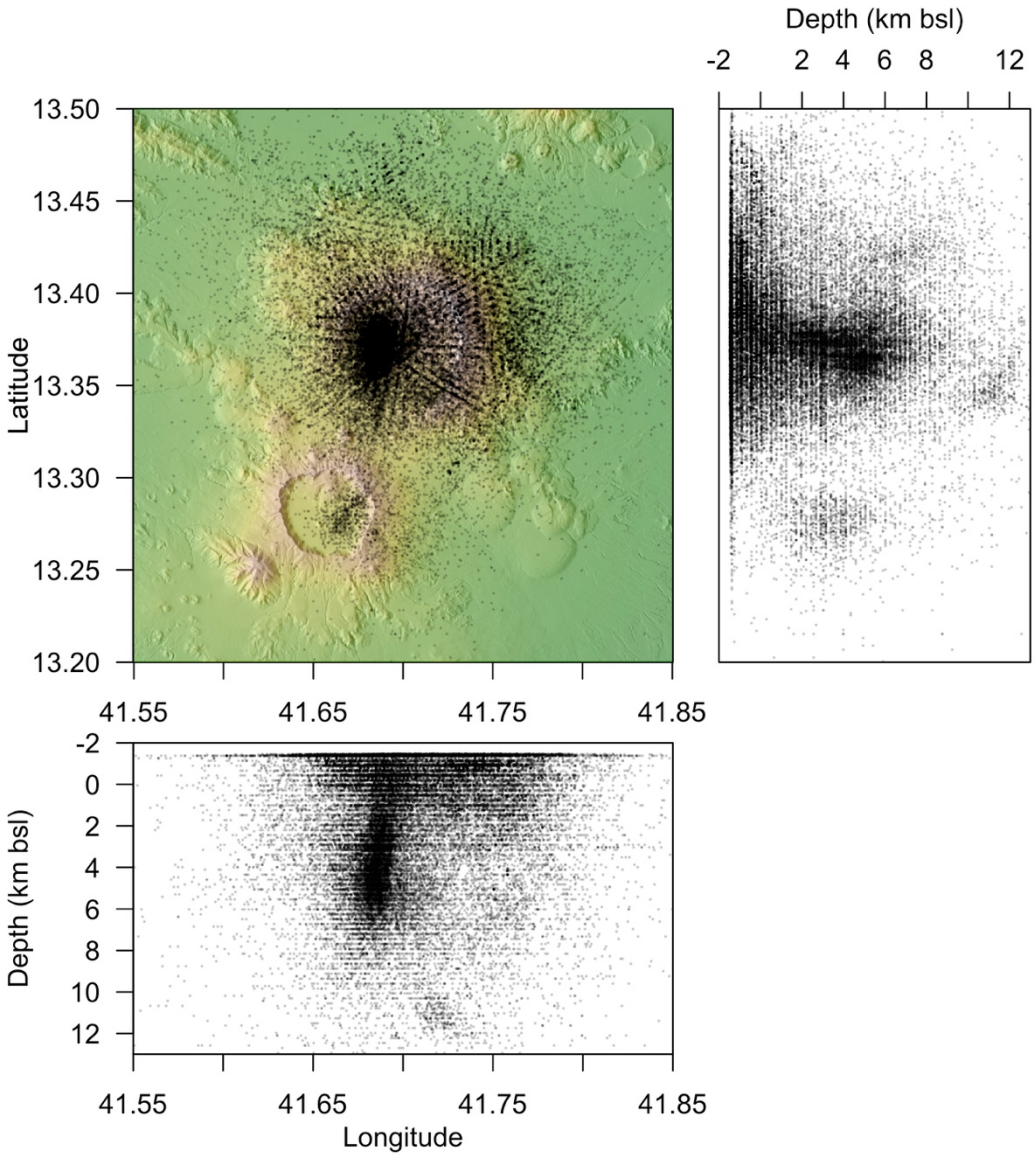

Figure S4. Event locations using P- and S-wave phase arrivals detected by original GPD model with 0.9 threshold (no. of events = 41,007).

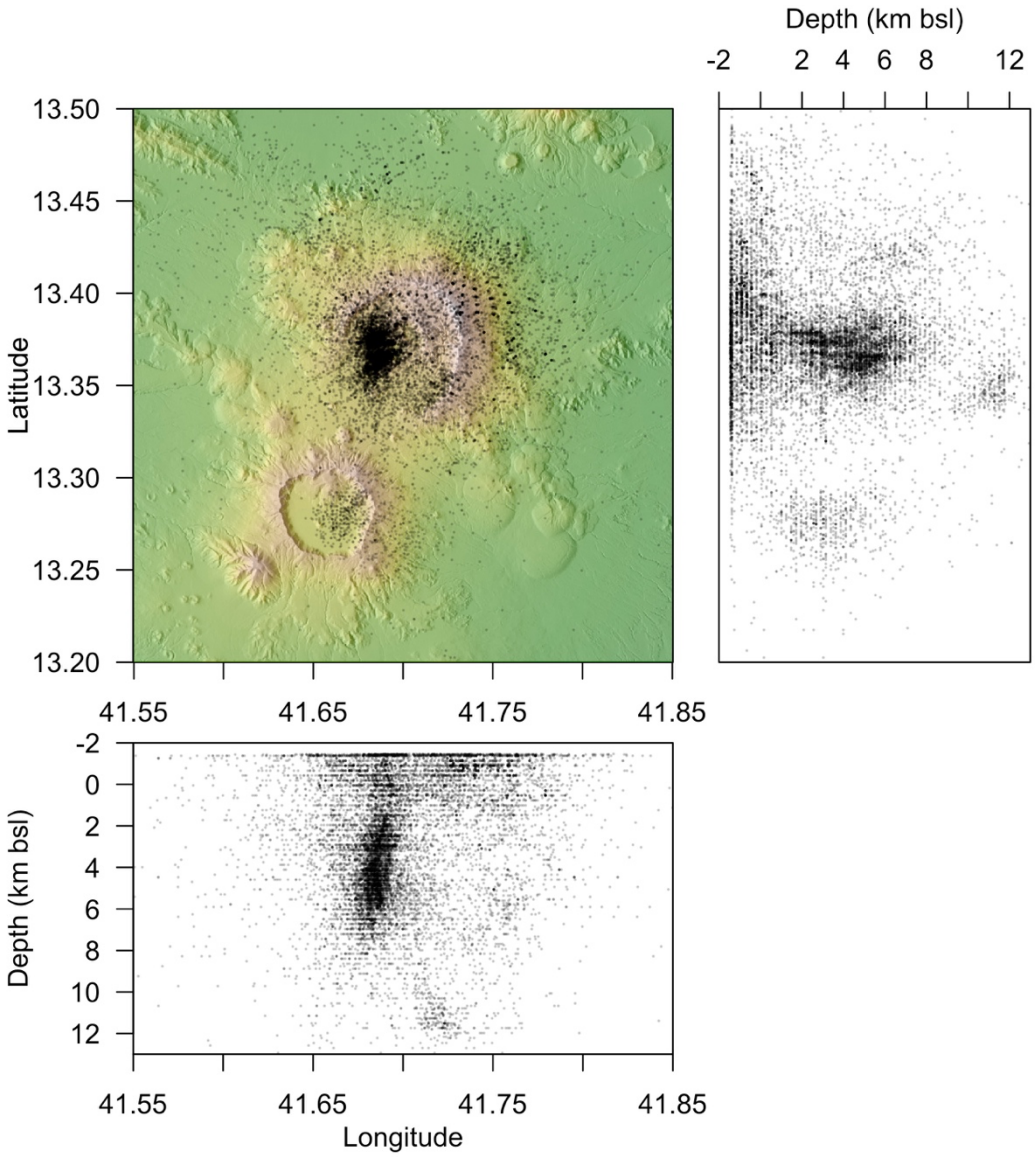

Figure S5. Event locations using P- and S-wave phase arrivals detected by original GPD model with 0.99 threshold (no. of events = 13,319).

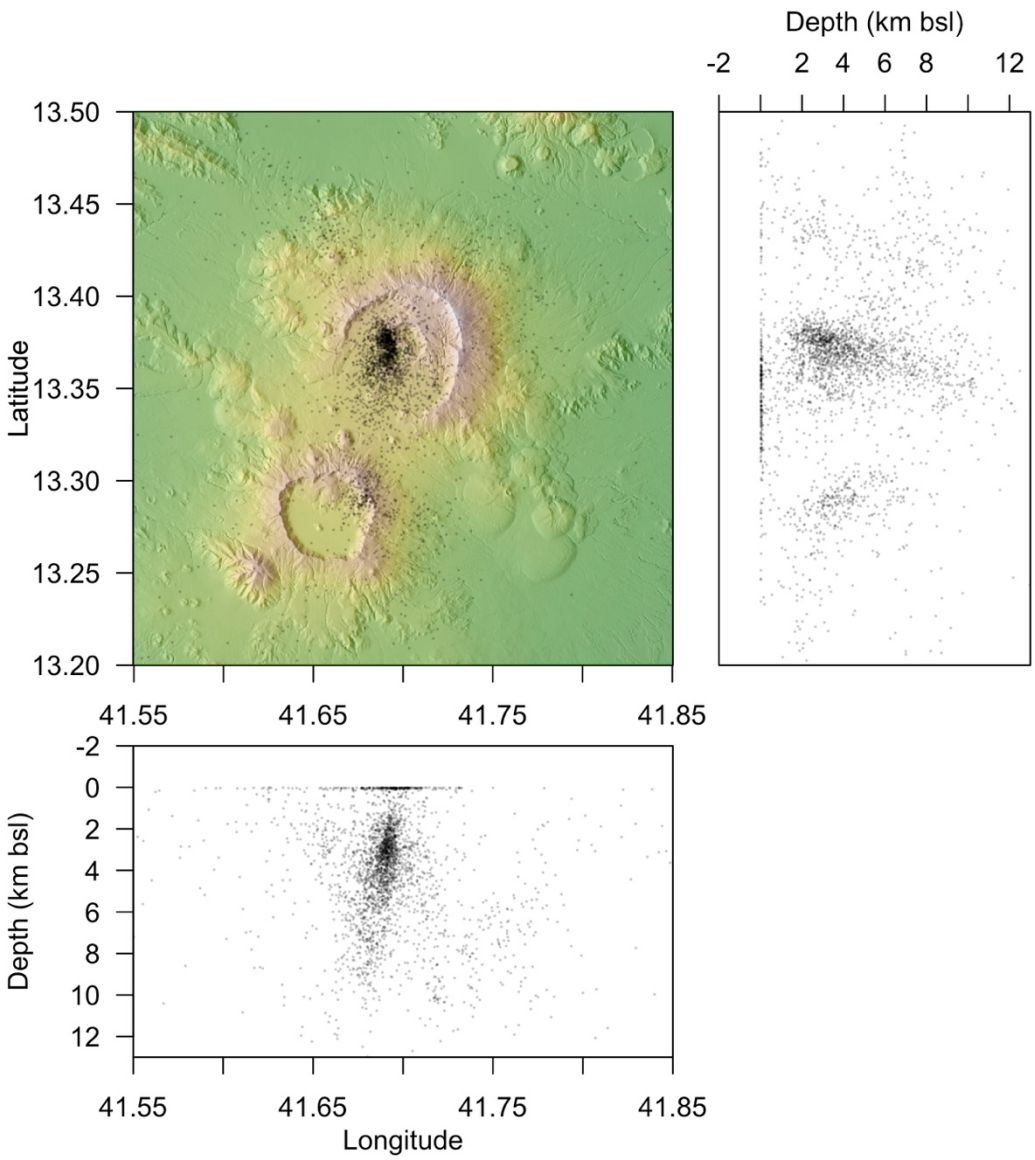

Figure S6. Event locations using P- and S-wave phase arrivals from original manual catalogue (no. of events = 2,984).

Text S7.

Supervised deep learning models are optimized through minimizing a loss function that measures the distance between the model's prediction and ground truth labels. To train our U-GPD transfer learning model, we use a cross entropy loss function, defined as:

$$\boldsymbol{L(p,q) = -\sum_{i=1}^{3}\sum_{x} p_i(x) \log q_i(x)}$$

where $\boldsymbol{i}$ is class/channel number (P, S or N), $\boldsymbol{x}$ are the datapoints in our waveform, $\boldsymbol{p_i(x)}$ is the ground truth probability distribution for $\boldsymbol{x}$ and $\boldsymbol{q_i(x)}$ is the model's predicted distribution for $\boldsymbol{x}$. The value of this loss function decreases as the model predictions converge towards the ground truth labels.

Table S8. P-wave 1D velocity model used to associate model phase arrival picks and locate events (linear gradient between layers, assumed Vp/Vs ratio of 1.76 for S-wave velocity model).

Depth for top of layer (km b.s.l.)	Vp (km / s)
-1.5	4.10
3.0	6.10
8.0	6.80
25.0	7.40